JOURNAL OF GEOPHYSICAL RESEARCH: SPACE PHYSICS, VOL. 118, 2593–2617, doi:10.1002/jgra.50249, 2013

Numerical modeling of the large-scale neutral and plasma responses to the body forces created by the dissipation of gravity waves from 6 h of deep convection in Brazil

S. L. Vadas[1] and H.-L. Liu[2]

Received 4 September 2012; revised 22 March 2013; accepted 22 March 2013; published 21 May 2013.

[1] We study the response of the thermosphere and ionosphere to gravity waves (GWs) excited by 6 h of deep convection in Brazil on the evening of 01 October 2005 via the use of convective plume, ray trace, and global models. We find that primary GWs excited by convection having horizontal wavelengths of $\lambda_H \sim$ 70–300 km, periods of 10–60 min, and phase speeds of $c_H \sim$ 50–225 m/s propagate well into the thermosphere. Their density perturbations are $\rho'/\overline{\rho} \sim$ 15–25% at $z \sim$ 150 km and are negligible at $z >$ 300 km. The dissipation of these GWs creates spatially and temporally localized body forces with amplitudes of 0.2–1.0 m/s^2 at $z \sim$ 120–230 km. These forces generate two counter-rotating circulation cells with horizontal velocities of 50–350 m/s. They also excite secondary GWs; those resolved by our global model have $\lambda_H \sim$ 4000–5000 km and $c_H \sim$ 500–600 m/s. These secondary GWs propagate globally and have $\rho'/\overline{\rho} \sim$ 10–25% and 5–15% at z = 250 and 375 km, respectively. These forces also create plasma perturbations of $f_oF2' \sim$ 0.2–1.0 MHz, TEC$' \sim$ 0.4–1.5 TECU (total electron content unit, 1 TECU = 10^{16} el m^{-2}), and $h_mF2' \sim$5–50 km. The large-scale traveling ionospheric disturbances (LSTIDs) induced by the secondary GWs have amplitudes of $f_oF2' \sim$ 0.2–0.5 MHz, TEC$' \sim$ 0.2–0.6 TECU, and $h_mF2' \sim$5–10 km. In a companion paper, we discuss changes to the prereversal enhancement and plasma drift from these forces.

Citation: Vadas, S. L., and H.-L. Liu (2013), Numerical modeling of the large-scale neutral and plasma responses to the body forces created by the dissipation of gravity waves from 6 h of deep convection in Brazil, *J. Geophys. Res. Space Physics*, *118*, 2593–2617, doi:10.1002/jgra.50249.

1. Introduction

[2] Gravity waves (GWs) have been observed in the thermosphere and ionosphere for decades [*Hocke and Schlegel,* 1996; *Crowley et al.*, 1987; *Oliver et al.*, 1997; *Djuth et al.*, 2004; *Shiokawa et al.*, 2006; *Nicolls and Heinselman*, 2007; *Nicolls et al.*, 2012; *Crowley and Rodrigues*, 2012]. Sources include the aurora [*Richmond*, 1978; *Hickey and Cole*, 1988; *Nicolls et al.*, 2012], deep convection [*Röttger*, 1977; *Hocke and Tsuda*, 2001; *Vadas and Crowley*, 2010; *Fukushima et al.*, 2012], hurricanes and tornados [*Bauer*, 1958; *Hung and Kuo*, 1978; *Bishop et al.*, 2006], nuclear explosions [*Harkrider*, 1964], tsunamis [*Occhipinti et al.*, 2006, 2008, 2011; *Hickey et al.*, 2009; *Rolland et al.*, 2010], and mountain wave breaking [*Vadas and Nicolls*, 2009].

[3] Deep convection occurs when moist air becomes unstable to small vertical movements [*Holton and Alexander*, 1999; *Piani et al.*, 2000; *Lane et al.*, 2001; *Horinouchi et al.*, 2002]. Such motions can excite GWs and acoustic waves. Because typical updraft velocities of convective plumes are $\sim$ 20–40 m/s with a maximum of $\sim$ 80–90 m/s and because the sound speed is 310 m/s, the excited GWs have much larger amplitudes (and energy) than the excited acoustic waves. We dub these GWs “primary GWs” because they are excited directly by deep convection.

[4] The spectrum of primary GWs excited by a single plume is quite rich, encompassing a large range of scales, $\lambda_H \sim$ 1–300 km, and phase speeds, $c_H \sim$5–250 m/s [*Pierce and Coroniti*, 1966; *Holton and Alexander*, 1999; *Lane et al.*, 2001; *Song et al.*, 2003; *Choi et al.*, 2007; *Vadas et al.*, 2009a, 2009b]. Because the density of the atmosphere decreases exponentially with altitude, a GW’s amplitude increases exponentially with altitude [*Hines*, 1960]. Although GWs with small horizontal wavelengths of $\lambda_H \sim$ 1–20 km tend to reach critical levels [*Preusse et al.*, 2008] or break in the stratosphere and mesosphere because their amplitudes become large there [*Lane et al.*, 2003], many medium-scale GWs have small-enough amplitudes in the upper mesosphere (i.e., nondimensional amplitudes less than 1) to allow them to propagate into the thermosphere if they can avoid critical levels and evanescence/reflection. Once in the thermosphere, they are subject to damping from

[1]NWRA/CoRA office, Boulder, Colorado, USA.
[2]National Center for Atmospheric Research (HAO/NCAR), Boulder, Colorado, USA.

Corresponding author: S. L. Vadas, NWRA/CoRA office, 3380 S. Mitchell Lane, Boulder, CO 80301, USA. (vasha@cora.nwra.com)

2169-9380/13/10.1002/jgra.50249

molecular viscosity and thermal diffusivity [*Pitteway and Hines*, 1963; *Hickey and Cole*, 1987; *Vadas*, 2007]. Because this damping increases nearly exponentially with altitude, it will eventually damp out every GW from the lower atmosphere. However, the dissipation altitude, z_{diss}, depends sensitively on a GW's parameters; those GWs with large vertical wavelengths λ_z and large intrinsic horizontal phase speeds c_{IH} survive to the highest altitudes [*Vadas*, 2007].

[5] GW dissipation in the thermosphere has several profound effects. First, it creates nonzero momentum flux divergence [*Kundu*, 1990], which serves to accelerate/decelerate the fluid on scales larger than λ_H [*Vadas and Fritts*, 2004, 2006]. Second, it causes heating/cooling of the fluid [*Walterscheid*, 1981; *Liu*, 2000; *Becker*, 2004; *Yiğit and Medvedev*, 2009; *Vadas*, 2013]. Both effects excite a second set of GWs in the thermosphere [*Zhu and Holton*, 1987; *Vadas and Fritts*, 2001; *Vadas and Liu*, 2009; *Vadas*, 2013]. We dub these latter GWs "secondary GWs" because they are created from the dissipation of primary GWs.

[6] Secondary GWs from deep convection have different spectral properties than the primary GWs which created them. This is primary due to wave dispersion. The secondary GW spectrum from deep convection in Tropical Storm Noel was quantified in *Vadas and Crowley* [2010] via reverse ray tracing the GWs detected at the bottomside of the *F* layer. The secondary GW spectrum had λ_H = 100–2000 km and c_H = 100–700 m/s, with peaks at $\lambda_H \geq$ 100–300 km and c_H = 100–300 m/s. These peak scales overlapped significantly with the peaks of the primary GW spectrum which survived to $z \sim$ 150–200 km. They argued that the secondary GW peak occurred at medium (rather than large) scales because of the medium-scale variability of the body forces created by the constructive/destructive interference of GWs from *multiple* convective plumes.

[7] *Vadas and Liu* [2009] calculated the thermospheric body force created by the dissipation of primary GWs from a single, deep convective plume on 01 October 2005 during the SpreadFEx campaign in Brazil. They then inserted this temporally and spatially localized force into the high-resolution Thermosphere-Ionosphere-Mesosphere-Electrodynamics General Circulation Model (TIME-GCM). They found that fast secondary GWs with $c_H \sim$ 500 m/s and $\lambda_H \sim$ 2100 km were excited by the body forces created by that single plume. Note that $\lambda_H \sim$ 2000 km is the minimum wavelength that the high-resolution TIME-GCM can effectively resolve. These secondary GWs propagated to the top of the model at $z \sim$ 450 km and had amplitudes which agreed well with typical DE2 and CHAMP satellite observations. This force also created total electron content (TEC) perturbations as large as $\sim$ 8% and large neutral horizontal wind perturbations of $\sim$ 200 m/s at $z \sim$ 180 km.

[8] The *Vadas and Liu* [2009] modeling study was recently significantly generalized by modeling the response of the thermosphere to *hundreds* of deep convective plumes and objects which occurred in Brazil over a 6 h period that same night. A brief and lightly peer-reviewed paper reported the local changes which occurred in the thermosphere near the bottomside of the *F* layer as a result of that convection [*Vadas and Liu*, 2011].

[9] This paper contains a much more comprehensive and detailed presentation of that same modeling study. It describes the local and global responses of the thermosphere and ionosphere to these same hundreds of convective plumes and objects which occurred that night. This study utilizes three numerical models. The first is a convective plume envelope model which calculates the analytic Fourier-Laplace GW solutions to an updraft of fluid in the troposphere. The second is a dissipative ray trace model which ray traces the primary GWs obtained from these analytic solutions (with their phases) into the thermosphere and calculates the forcings where these GWs dissipate in the thermosphere. The third is the TIME-GCM which calculates the excited secondary GWs and LSTIDs and calculates the large-scale neutral wind, temperature, and density changes (such as the counter-rotating cells). Of these three models, only the TIME-GCM is a direct numerical simulation (DNS). One of the purposes of the first two models is to provide realistic, spatially and temporally varying, subgrid-scale, convective forcings associated with the primary GWs as input into the TIME-GCM, since the TIME-GCM cannot resolve the primary GWs directly. This allows for the determination of the global responses of the thermosphere and ionosphere to GWs from deep convection.

[10] In section 2, we describe the excitation and propagation of primary GWs from deep convective plumes and objects (identified from satellite images) into the thermosphere using our convective plume and dissipative ray trace models. We then reconstruct the GW fields in the thermosphere and calculate average GW parameters. Section 3 shows the body forces (or accelerations) created in the thermosphere where these primary GWs dissipate. In section 4, we input these forces into the TIME-GCM and show the excited secondary GWs and LSTIDs, along with the neutral wind/temperature/density changes. Our conclusions are provided in section 5. A companion paper discusses changes to the prereversal enhancement and plasma drift as a results of these body forces [*Liu and Vadas*, 2013].

2. Generation and Propagation of Primary GWs From Deep Convection

[11] Over the past few decades, many numerical models have been developed to simulate the GWs excited by deep convection [e.g., *Holton and Alexander*, 1999; *Pandya and Alexander*, 1999; *Horinouchi et al.*, 2002; *Lane et al.*, 2003]. Within a moist convective system, both diabatic forcing (i.e., latent heating and cooling) and nonlinear forcing excite GWs [*Lane et al.*, 2001]. Since these sources are largely out of phase with one another, linear dry GW excitation models which include only one of these sources must reduce the excited GW amplitudes by $\sim$ 2 and must only include GWs with horizontal phase speeds $c_H >$ 20–25 m/s [*Song et al.*, 2003; *Choi et al.*, 2007]. Currently, there are linear "dry-air" GW excitation models which implement (1) diabatic forcing [*Alexander et al.*, 1995; *Piani et al.*, 2000; *Walterscheid et al.*, 2001; *Beres*, 2004] and (2) convective overshoot [*Stull*, 1976; *Vadas and Fritts*, 2009]. GW excitation from deep convection excites high-frequency GWs with $\lambda_H \sim$ 1 km to hundreds of kilometers and with periods of 5 min to a few hours.

[12] Our convective plume model is an idealized, linear model which implements the latter process [*Vadas and Fritts*, 2009]; it models the envelope of a 3-D convective plume as a Gaussian, vertical body force, thereby

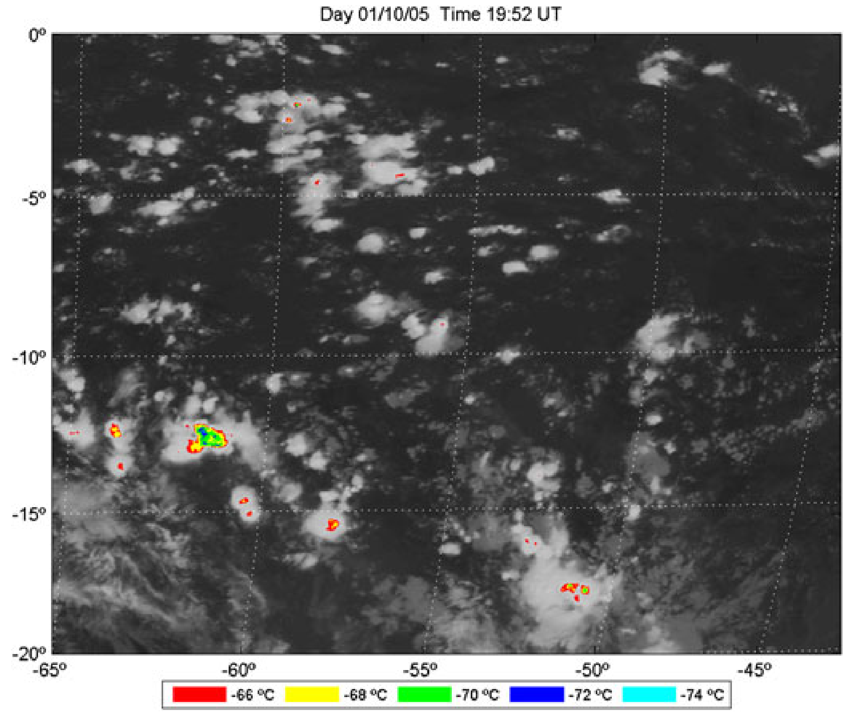

Figure 1. Goes-12 infrared satellite image at 19:52 UT of Brazil. White dotted lines represent longitude (x axis) and latitude (y axis) lines. Colors denote temperatures (in Celsius).

neglecting the small-scale processes which create small-scale GWs. Since very-small-scale GWs cannot propagate above the stratopause, this model is appropriate for mesospheric and thermospheric GW studies for small to medium-scale GWs with $c_H > 20$ m/s. This model is not a DNS; instead, it uses analytic, Fourier-Laplace solutions to determine the excited, linear, GW spectrum as a function of wavevector (k, l, m) [*Vadas and Fritts*, 2001]. Each Gaussian force has a full diameter of $\mathcal{D}_H$ and a full depth of $\mathcal{D}_z$. The grid spacings are chosen to be $\Delta_x = \Delta_y = (\mathcal{D}_H/2.25)$ in the x and y directions and $\Delta_z = (\mathcal{D}_z/2.25)$ in the z direction. Thus, each Gaussian force contains a total of $\sim 2.25^3 \sim 11$ grid points. Note that this grid can only "resolve" GWs with $\lambda_i \geq 2\Delta_i$ [*Vadas and Fritts*, 2009]. (Thus, for a convective plume with a diameter of 20 km and a depth of 10 km, the grid point spacings are $\Delta_x = \Delta_y = 8$ km and $\Delta_z = 2$ km, and we can "resolve" GWs with $\lambda_x, \lambda_y \geq 16$ km and $\lambda_z \geq 4$ km.) We then take the Fourier transform of this Gaussian vertical body force and compute the analytic GW solutions as a function of wavevector. These solutions yield the amplitudes and phases of the primary GWs excited by this idealized plume.

[13] We then utilize an anelastic, dissipative GW ray trace model, which propagates the excited primary GWs (with their phases) into the mesosphere and thermosphere using an explicit, fourth-order Runge Kutta routine [*Press et al.*, 1992]. This model utilizes a GW dispersion relation which incorporates the dissipation of a GW in the thermosphere from kinematic viscosity and thermal conductivity [*Vadas and Fritts*, 2005]. It does not include the Coriolis force. In the limit that GW dissipation is negligible, this dispersion relation reduces to the usual anelastic dispersion relation given by *Eckermann and Marks* [1996] with zero Coriolis force ($f = 0$). The approximation $f \sim 0$ is adequate for the primary convective GWs, because their periods are less than an hour. Note that this ray trace model allows for the variation of the background wind, density, and temperature in space and time. Further details of both models can be found below and in *Vadas et al.* [2012].

[14] GOES-12 satellite images color-coded in temperature from –66°C to –74°C and covering 45°W–65°W and 0°S–20°S in central Brazil are available every 30 min during the 6 h period from 18:22–23:53 UT on 01 October 2005 [*Vadas et al.*, 2009a]. Since the local time (LT) is LT = UT – 3 h in mid-Brazil, this includes sunset at ~22:30 UT. Deep convection peaked at 19:00–22:00 UT and weakened rapidly after 23:00 UT. Using balloon soundings, the tropopause temperature is determined to be ~ 209K. All plumes colder than this temperature likely underwent convective overshoot (i.e., punched into the stratosphere where the temperature increases with altitude) and therefore are identified as generating GWs. Figure 1 shows an example image at 19:52 UT. Images at 18:52, 20:53, 21:22, 21:52, and 22:22 UT are shown in *Vadas et al.* [2009a]. All told, 136 convective objects are identified; each is classified as a single convective plume, a convective cluster containing two or more tightly clumped convective plumes, or a convective complex with two or more less-tightly clumped convective plumes. Clusters are defined as three identical plumes at the corners of a triangle, with adjacent plume centers separated by $2.5\mathcal{D}_H$, where $\mathcal{D}_H$ is the diameter of each plume. Complexes are defined as four identical plumes at the corners of a square, with adjacent plume centers separated by $4.5\mathcal{D}_H$.

[15] Figure 2 shows a sketch of the locations, times, types, average plume diameters, and updraft velocities of the 136 convective objects identified from these images. The most common object is a single plume; however, there are 33 clusters and 22 complexes. The average plume diameter ranges

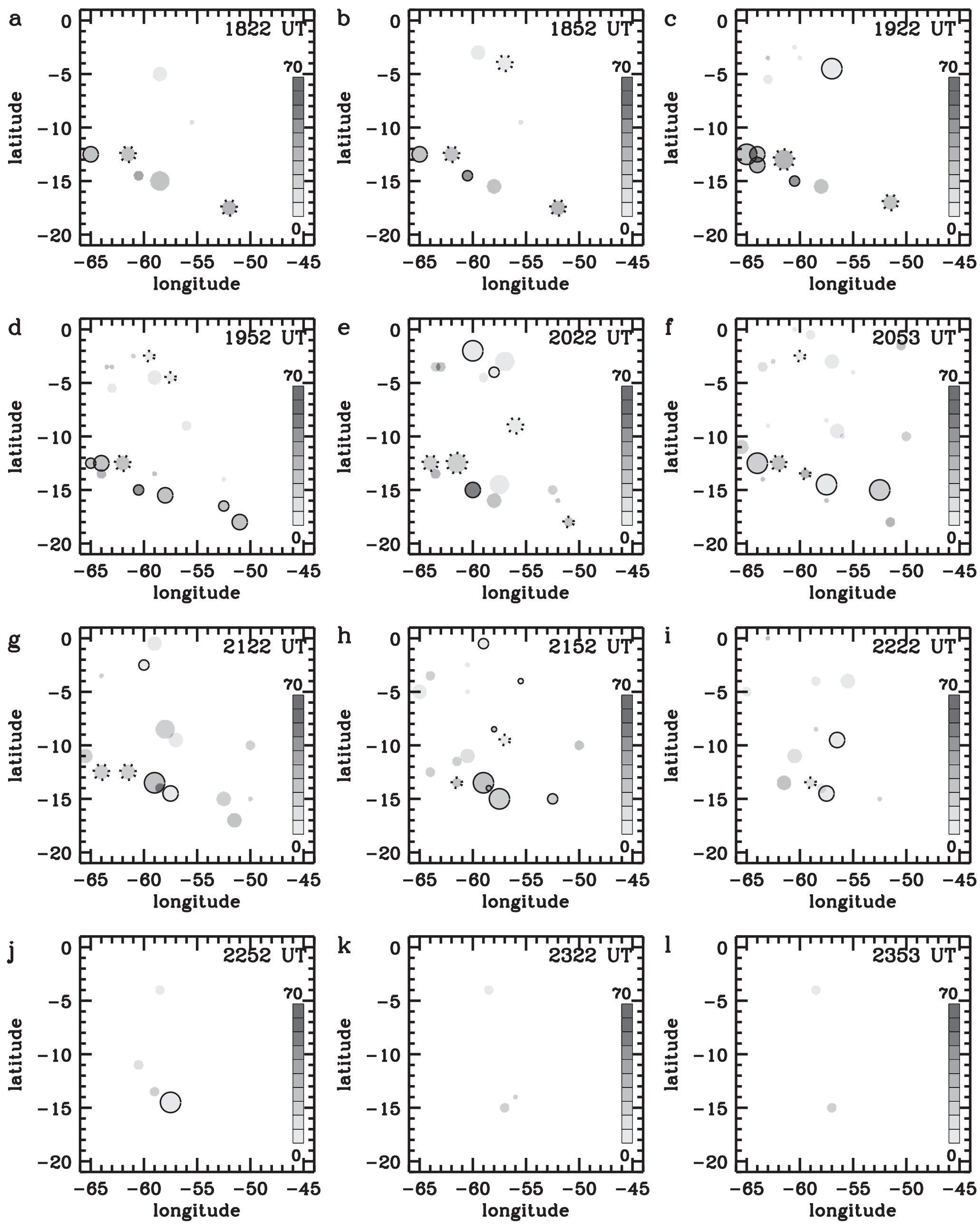

Figure 2. Locations, updraft velocity w_{pl}, and types of convective objects from 18:22 to 23:53 UT, as labeled. Shaded circles denote single plumes. Solid (dotted) lines surrounding shaded circles denote clusters (complexes). The amount of shading denotes w_{pl} on a linear scale from 0 to 70 m/s (gray color bars). The diameter of each shaded circle is $10\mathcal{D}_H$ for illustration purposes, where $\mathcal{D}_H$ is the average plume diameter within an object. For example, although the cluster at 57.5°W, 14.5°S, and 22:52 UT contains plumes with $\mathcal{D}_H$ = 20 km, it is shown with a diameter of 200 km.

from $\mathcal{D}_H$ = 5 to 20 km. The plume updraft velocities, w_{pl}, are estimated from Convective Available Potential Energy (CAPE) maps [*Vadas and Crowley*, 2010] and range from $w_{\mathrm{pl}} \simeq 0$ to 63 m/s. Because the primary and secondary GW amplitudes are proportional to w_{pl} and w_{pl}^2, respectively, we only simulate those objects with $w_{\mathrm{pl}} \geq 10$ m/s here. Examples of primary GW spectra excited by plumes and clusters are shown in *Vadas et al.* [2009a]. A convective plume typically lasts ∼ 15 min before collapsing. Afterward, because the troposphere in the vicinity of the collapsed plume remains unstable with significant potential energy, other convective plumes are typically formed near the outer edge of the original plume. Because we do not have images every 15 min (when new convective plumes would excite additional GWs), we assume that the same convective objects occur at the same locations (with the same diameters and updrafts velocities) 15 min after each satellite image. This allows us to more fully estimate the effect on the thermosphere from all anticipated convective activity during this 6 h period.

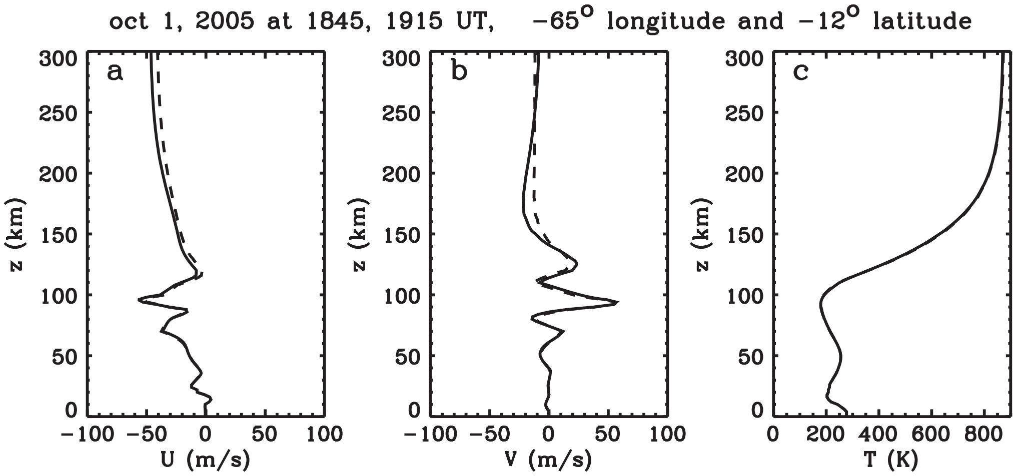

Figure 3. Background (a) zonal wind, (b) meridional wind, and (c) temperature at 65°W and 12°S at 18:45 (solid) and 19:15 (dashed) UT as a function of altitude.

[16] The primary GWs excited by each convective object are then ray traced into the thermosphere through varying background wind and temperatures. Such a scheme assumes that the GW amplitudes are linear (except for saturation—see below). The background wind and temperatures are determined from balloon soundings, meteor winds, and the TIME-GCM, as described in *Vadas et al.* [2009a]. Figure 3 shows the background wind and temperature at 65°W and 12°S at 18:45 and 19:15 UT. The wind is approximately northwestward at $z \sim 120$–150 km and is westward for $z > 200$ km. The wind amplitude and direction is approximately constant for $z > 200$ km, because the diurnal tide is damped from molecular viscosity. The ray-traced GW parameters (such as momentum flux, wavevector, phase) are saved in a 4-D grid with cell sizes 50 km × 50 km × 4 km × 10 min in x, y, z, and t. Because this model is not a DNS, the purpose of this grid is to add up the effects of each GW as it propagates cell to cell. The GW fields (such as the velocity perturbations (u', v', w') and density perturbations ρ') are then reconstructed from this 4 D grid [*Vadas and Fritts*, 2009]. We also include the effects of parameterized wave breaking from both single [*Lindzen*, 1981] and multiple waves [*Smith et al.*, 1987]. Here, we calculate $A^2 = \Sigma_i A_i^2$ in each (x, y, z, t) cell; if this value exceeds one, we reduce the amplitudes of all i GWs at this location and time so that the sum equals 1. Here, A_i is the ith GW's horizontal wave amplitude scaled by its respective intrinsic phase speed (i.e., its nondimensional amplitude). Parameterized wave breaking is included by running the ray trace model a second time for all convective objects. These effects are now known to be important in the thermosphere for large-amplitude waves [*Yiğit et al.*, 2008, 2009]. Without this effect, the nondimensional wave amplitudes A in this study would have been unrealistically large, up to $A \sim 5$–20. Including this effect decreases somewhat the altitude where the thermospheric body forces are maximum. Parameterized wave breaking has the effect of altering the background flow via the deposition of momentum. Such accelerations also excite secondary GWs.

[17] Figure 4 shows the density perturbations of the primary GWs at $z = 150$ and $z = 250$ km at various times throughout the evening, starting an hour after convection is modeled. At $z = 150$ km, $\rho'/\overline{\rho} \sim 15$–25%. These amplitudes are only slightly larger than the thermospheric density perturbations created from the GWs excited by the single, weaker plume (with $w_{\rm pl} = 35$ ms^{-1}) simulated by *Vadas and Liu* [2009]. (Note that parameterized wave breaking was not included in *Vadas and Liu* [2009].) This similarity might seem counterintuitive, because the current simulation has numerous plumes with much larger updraft velocities. However, wave saturation (applied here) limits the amplitude growth for GWs with large amplitudes and for multiple GWs constructively interfering; this causes $A \sim 1$. Additionally, post-processing of the *Vadas and Liu* [2009] results shows that $A \sim 1$ for the primary GWs in that simulation. This is why the density perturbations from the hundreds of strong plumes simulated here approximately equal the density perturbations from the single, weaker plume simulated in *Vadas and Liu* [2009]. We note that because $A \sim 1$ for the primary GWs in *Vadas and Liu* [2009], parameterized wave breaking would not have changed those results significantly; therefore, those results are still valid.

[18] Figure 4 shows that the primary GWs have $|\rho'/\overline{\rho}| \sim 15$–25% and form partial concentric rings at $z = 150$ km (Figures 4a–4f). Each set of concentric rings is from a different convective object. As time progresses (left to right), the GW horizontal wavelengths decrease from $\lambda_H \sim 200$ km (Figure 4a) to $\lambda_H \sim 100$ km (Figure 4f). This is due to wave dispersion: those GWs with large λ_z and λ_H have larger vertical group velocities than those GWs with smaller λ_z and λ_H and therefore reach the thermosphere earlier. At $z = 250$ km (Figures 4g–4l), $\rho'/\overline{\rho} \sim 1$–2%, and the rings are no longer visible because of wind and dissipative filtering. Instead, the GW phase lines appear as approximately parallel lines. As time progresses, the GW horizontal wavelengths decrease from $\lambda_H \sim 300$ km (Figure 4g) to $\lambda_H \sim 200$ km (Figure 4l). Note that the GW propagation direction is perpendicular to the phase lines.

[19] Figure 5 shows horizontal slices of the temperature perturbations, T', created by the primary GWs at $z = 150$ and 200 km. The background temperature $\overline{T}$ at $z = 150$ and

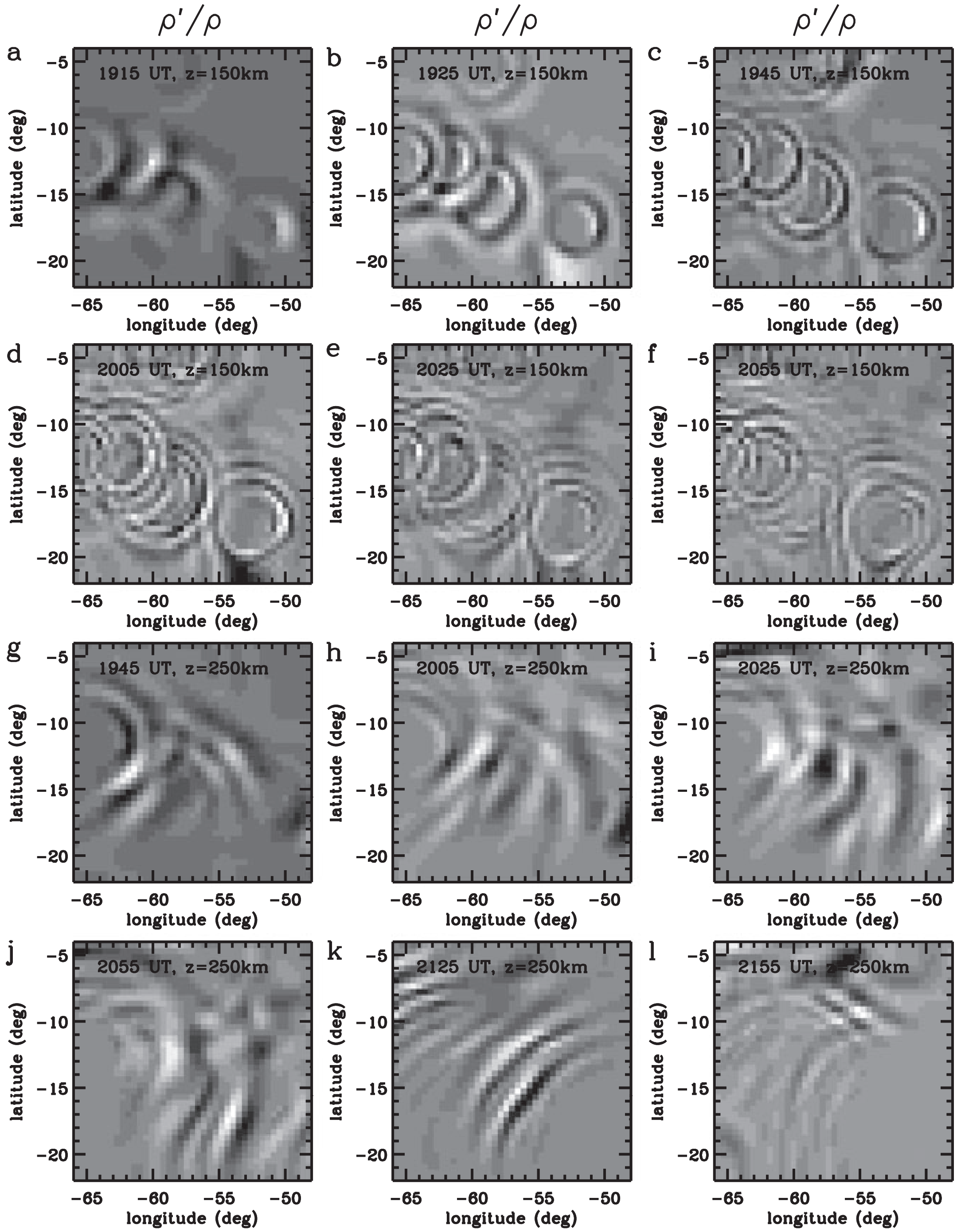

Figure 4. Horizontal slices of the reconstructed primary GW density perturbations, $\rho'/\overline{\rho}$ (a–f) at z = 150 km and (g–l) at z = 250 km. Figures 4a – 4f show 19:15, 19:25, 19:45, 20:05, 20:25, and 20:55 UT. Figures 4g – 4l show 19:45, 20:05, 20:25, 20:55, 21:25, and 21:55 UT. The maximum values of $|\rho'/\overline{\rho}|$ are 23, 15, and 24% (in Figures 4a – 4c); 18, 23, and 21% (in Figures 4d – 4f); 2, 2, and 1% (in Figures 4g – 4i); and 2, 2, and 0.3% (in Figures 4j – 4l).

200 km is ~625 and ~825 K, respectively. We see that the primary GWs have large perturbations of $|T'| \sim$ 50–100 K ($T'/\overline{T} \sim$ 8–16%) at z = 150 km and 19:25–23:25 UT. This is an hour after deep convection becomes strong (i.e., after the plume updraft velocities become relatively large). The temperature perturbations, $T'/\overline{T}$, have amplitudes that are similar to the density perturbation amplitudes, $\rho'/\overline{\rho}$, in Figure 4, because the pressure perturbations are small. At z = 150 km and 19:25 UT, note that the GWs are propagating primarily southeastward from convective plumes in the vicinity of 55°W–65°W and 12°S–17°S. Additionally, their phase lines retain some of their original concentric ring structure. From Figure 3, the background wind is northwestward at z = 120–150 km at somewhat earlier times. This result, that the GWs which most easily survive thermospheric dissipation propagate approximately against the wind, has

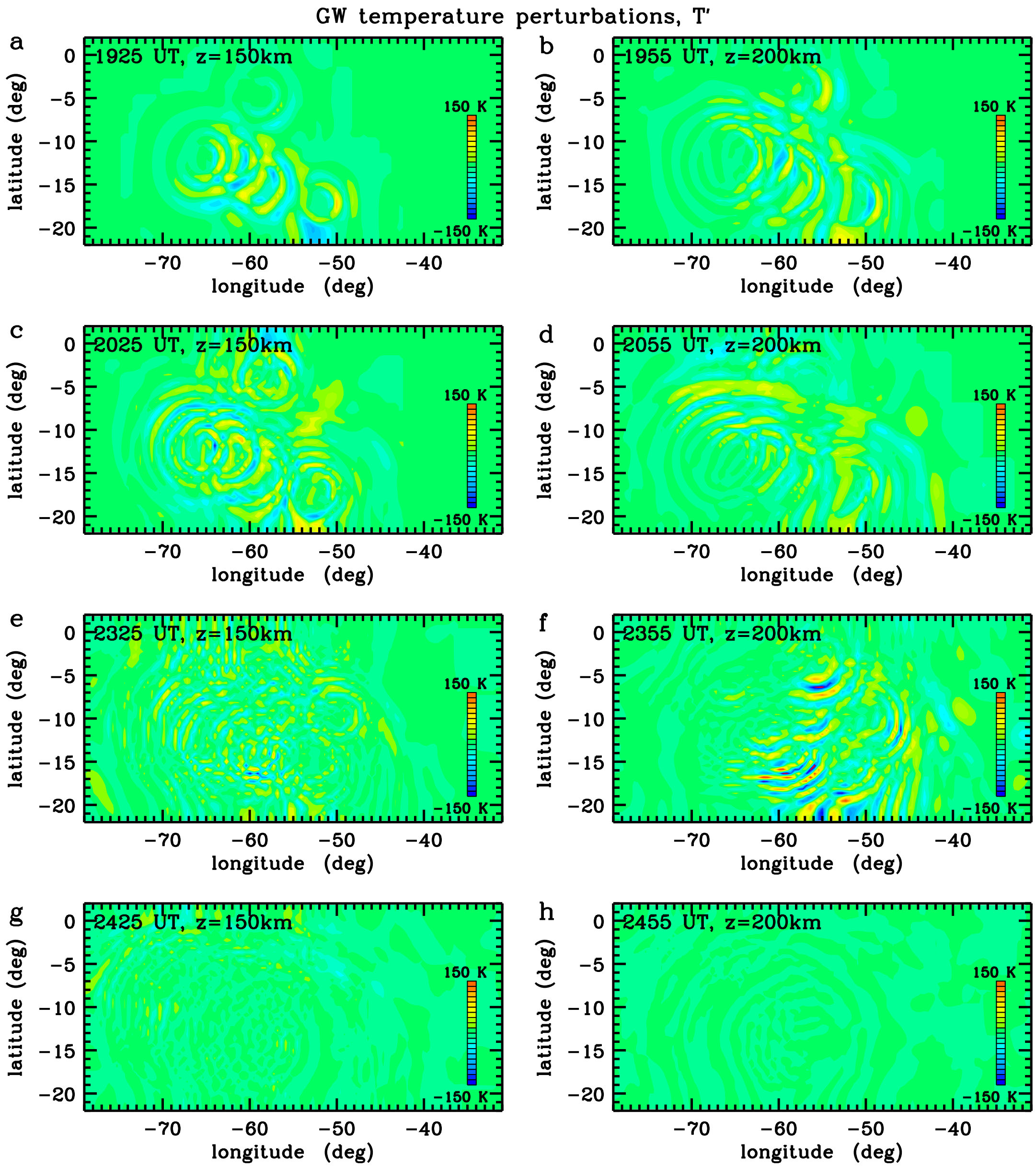

Figure 5. Horizontal slices of the reconstructed primary GW temperature perturbations, T', (a, c, e, g) at z = 150 km and (b, d, f, h) at z = 200 km. Figures 5a–5h show 19:25, 19:55, 20:25, 20:55, 23:25, 23:55, 24:25, and 24:55 UT, respectively. The colors denote T' on a linear scale from –150 to 150 K.

been reported previously [*Sun et al.*, 2007; *Fritts and Vadas*, 2008; *Crowley and Rodrigues*, 2012].

[20] At z = 200 km and 23:55 UT, the temperature perturbations are quite large in Figure 5: $|T'| \sim$ 100–150 K. This may be due to a wind effect, since $T' \propto \omega_{Ir}^{-1}$ becomes large for GWs nearing critical levels [*Fritts and Alexander*, 2003; *Vadas et al.*, 2009b]. Figure 5 shows that the time scales for variability of T' is less than 30 min. Note that T' is relatively large until 24:00 UT. This corresponds to a few hours after the last large-$w_{\rm pl}$ convective plumes have overshot the tropopause (~22:00 UT from Figure 2).

[21] Figure 6 shows vector plots of the horizontal velocity perturbations induced by the primary GWs at the same altitudes and times as in Figures 5c and 5f. The perturbations are quite large at z = 150 km, where the maximum of $u'_H = \sqrt{(u')^2 + (v')^2}$ is 180 m/s. This is much larger than the background tidal winds [*Vadas et al.*, 2009a]. These wind perturbations are smaller at z = 200 km: u'_H = 60 m/s. Figure 7 shows the horizontal and vertical velocities induced by the primary GWs at z = 250 km at various times. This altitude is near the bottomside of the F layer (see section 4.2). Note that the horizontal velocities (~ 5–15 m/s) are much smaller at this altitude than at z = 150 and 200 km (see Figure 6). The vertical velocities are somewhat larger, $w' \sim$ 35 m/s.

[22] Figure 8 shows the zonal velocity perturbations induced by the primary GWs for the same altitudes and times as in Figure 5. The primary GW velocity perturbations are quite strong at z = 150–200 km, with magnitudes of 50–150 m/s. Additionally, magnitudes of ~ 50 m/s are quite

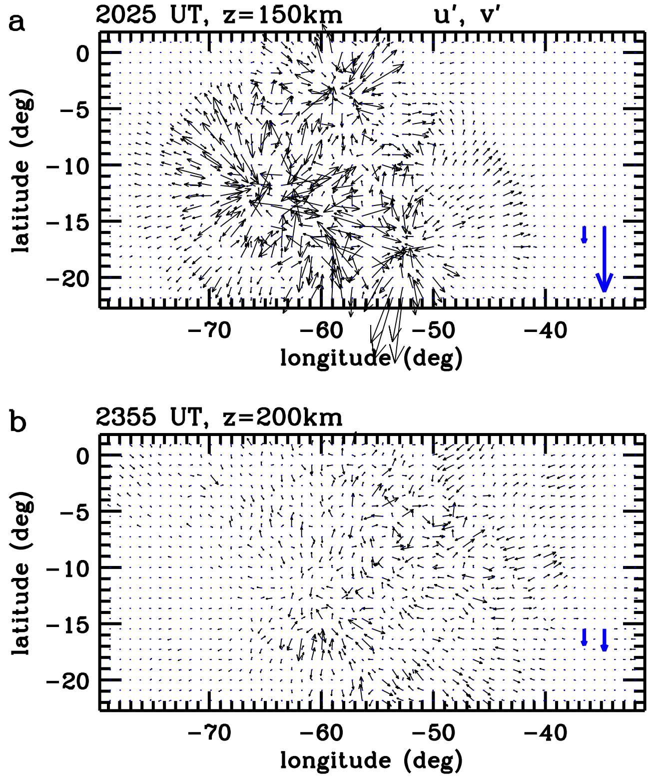

Figure 6. Reconstructed primary GW horizontal velocity perturbations at (a) z = 150 km and 20:25 UT and (b) z = 200 km and 23:55 UT. The direction of the arrows denote the wind direction, and the lengths are proportional to the speed. The maximum horizontal velocities are 180 m/s in Figure 6a and 60 m/s in Figure 6b. The downward blue arrows in the lower right-hand corner are scale vectors; the one to the right shows the magnitude of the maximum velocity in that panel, while the one to the left shows 40 m/s.

common during deep convection. Because the tidal winds have maximum values of ∼ 30–50 m/s at these times and altitudes [*Vadas et al.*, 2009a], we conclude that the primary GW velocities contribute significantly to the variability of the neutral winds at these altitudes.

[23] Figure 9 shows vertical slices of the primary GW temperature perturbations at 15°S. The slopes of the phase lines (which is a measure of $|\lambda_z|$) increases with altitude at all three times, as expected [*Vadas*, 2007]. In the midthermosphere ($z \sim 200$ km), $|\lambda_z| \sim 50$–60 km. However, in the lower thermosphere ($z \sim 110$–150 km), $|\lambda_z|$ is smaller (∼ 15–40 km). This is especially evident at somewhat later times when the slower GWs reach the lower thermosphere. Note that the GW amplitudes decrease rapidly with altitude for $z > 200$ km.

[24] We now calculate the average wave numbers and wave frequencies in each (x, y, z, t) cell, weighted by the vertical flux of horizontal momentum, e.g.,

$$\bar{k}(x,y,z,t) = \frac{\Sigma_i k_i \left(u'_H w'\right)_i}{\Sigma_i \left(u'_H w'\right)_i}, \qquad \bar{l}(x,y,z,t) = \frac{\Sigma_i l_i \left(u'_H w'\right)_i}{\Sigma_i \left(u'_H w'\right)_i}$$
$$\overline{m}(x,y,z,t) = \frac{\Sigma_i m_i \left(u'_H w'\right)_i}{\Sigma_i \left(u'_H w'\right)_i}, \qquad \overline{\omega_{Ir}}(x,y,z,t) = \frac{\Sigma_i (\omega_{Ir})_i \left(u'_H w'\right)_i}{\Sigma_i \left(u'_H w'\right)_i}. \tag{1}$$

Here, (k, l, m) is the local wavevector in geographic coordinates, $u'_H = \sqrt{(u')^2 + (v')^2}$, and the sum is over all of the GWs which enter this cell [*Vadas and Fritts*, 2009]. Here, overlines denote averages over one to two wave periods and wavelengths. Then, the average horizontal wave number is $\overline{k_H} = \sqrt{\bar{k}^2 + \bar{l}^2}$, the average horizontal wavelength is $\overline{\lambda_H} = 2\pi/\overline{k_H}$, the average intrinsic and observed phase speeds are $\overline{c_{IH}} = \overline{\omega_{Ir}}/\overline{k_H}$ and $\overline{c_H} = \overline{\omega_r}/\overline{k_H}$, and the average intrinsic and observed wave periods are $\overline{\tau_{Ir}} = 2\pi/\overline{\omega_{Ir}}$ and $\overline{\tau_r} = 2\pi/\overline{\omega_r}$.

[25] Figure 10 shows distributions of these average GW parameters at 19:25, 20:25, and 23:25 UT. The profiles at z = 150, 175, 200, and 225 km are offset along the y axis. The cells with very large average horizontal wavelengths of $\overline{\lambda_H} > 300$ km at z = 150 km are somewhat misleading, because they are created by GWs moving in different directions. Opposite propagation directions lead to partial cancelation of the $u'_H w'$ contributions in equation (1), resulting in smaller $\overline{k_H}$. At $z \geq 200$ km, $\overline{\lambda_H}$ is 70–300 km. These profiles are fairly invariant with altitude. As a general trend, $|\overline{\lambda_z}|$ increases significantly with altitude, as expected (see Figure 9), although this trend is most noticeable at the earliest times when $|\overline{\lambda_z}| \sim 80$–100 km. The intrinsic and observed horizontal phase speeds are ∼ 100–225 m/s. These values tend to decrease at later times. Altogether, the primary GW phase speeds include 50–225 m/s. Finally, the intrinsic and observed periods are ∼ 10–25 min at early times. These values increase to ∼ 15–40 min at late times, with a broad tail extending to periods of 80 min at $z \leq 200$ km.

3. Body Forces Induced by the Dissipation of Primary Convective GWs

[26] We now determine the body forces which accompany the dissipation and/or saturation of the primary convective GWs in the thermosphere. The effect of GW dissipation on the mean flow can be described by the horizontal components of the Reynolds stress tensor [*Bretherton*, 1969]. The zonal and meridional components of the body force in geographic coordinates (per unit mass) are [*Andrews et al.*, 1987; *Kundu*, 1990]

$$F_x = -\frac{1}{\bar{\rho}} \frac{\partial \left(\bar{\rho}\, \overline{u'w'^*}\right)}{\partial z}, \quad F_y = -\frac{1}{\bar{\rho}} \frac{\partial \left(\bar{\rho}\, \overline{v'w'^*}\right)}{\partial z}, \tag{2}$$

respectively. Here, * denotes complex conjugate, and overlines denote averages over several wavelengths. We compute the vertical divergences of the total zonal and meridional-momentum fluxes from the primary GWs excited by all convective plumes and objects. If the GWs are not dissipating or saturating, $\left(\bar{\rho}\, \overline{u'w'^*}\right)$ and $\left(\bar{\rho}\, \overline{v'w'^*}\right)$ are constant with altitude, so that $F_x = F_y = 0$.

[27] Because the TIME-GCM includes a GW parameterization scheme up to z = 120 km, we smoothly zero out the body forces below 120 km in order to avoid double counting the GW effects. We choose a smoothing range of δ = 20 km. For altitudes below z_i = 100 km, we set the body forces equal to zero. For altitudes between z_i and $z_i + \delta$, we multiply the body forces by

$$1 - \cos^2\left[\pi(z - z_i)/(2\delta)\right]. \tag{3}$$

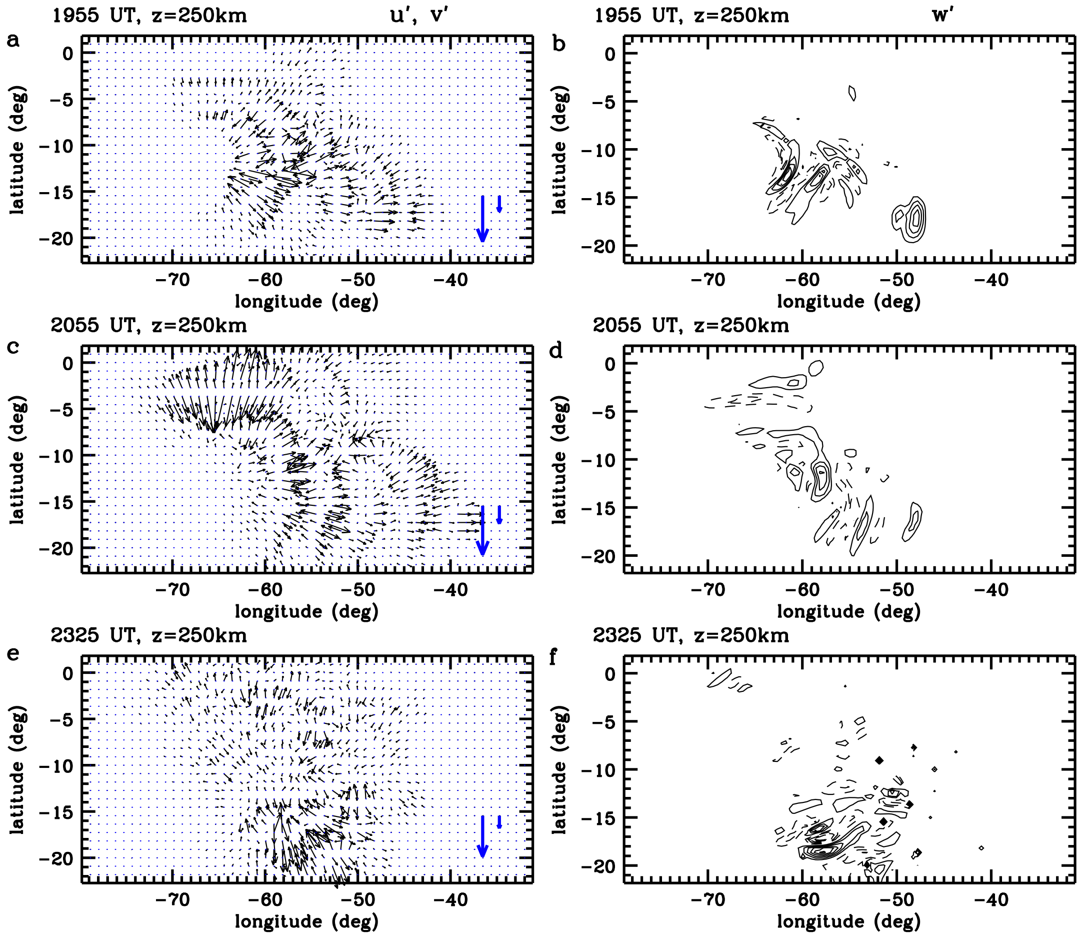

Figure 7. Horizontal slices of the reconstructed primary GW (a, c, e) horizontal velocity and (b, d, f) vertical velocity perturbations at z = 250 km. Times shown in the first, second, and third rows are 19:55 UT, 20:55 UT, and 23:25 UT, respectively. The maximum values of $|u'_H|$ are 13 m/s (in Figure 7a), 12 m/s (in Figure 7c), and 8 m/s (in Figure 7e). The blue arrows in Figures 7a, 7c, and 7e are the same as in Figure 6. The solid (dashed) lines in Figures 7b, 7d, and 7f denote positive (negative) values in intervals of 2 m/s. The maximum values of $|w'|$ are 10 m/s (in Figure 7b), 8 m/s (in Figure 7d), and 34 m/s (in Figure 7f).

We find that the largest value of F_x is eastward, F_x = 0.83m/s^2, and occurs at 60°W, 12°S, z = 152 km, and 19:15 UT. The largest value of F_y is southward, F_y = –0.89m/s^2, and occurs at 53°W, 20°S, z = 164 km, and 19:25 UT. These amplitudes are consistent with previous results from a single convective plume [*Vadas and Liu*, 2009]. However, the altitude of the thermospheric body forces are lower here by $\sim$ 25–35 km. This is due, in part, to the inclusion of wave saturation, to the constructive interference of GWs from multiple convective objects, and to the larger plume updraft velocities.

[28] Figures 11a–11f show horizontal slices of (F_x, F_y) at z = 150 km. The strongest accelerations last for 1.5 h, from 19:25 to 20:55 UT, and are east, south, and southeastward. The accelerations are patchy and variable because of constructive and destructive interference of GWs from different convective objects. GWs moving against the background wind propagate to higher altitudes in the thermosphere [*Fritts and Vadas*, 2008]. Those GWs which dissipate at z = 150 km are propagating in a direction which is opposite to the background wind direction one to two neutral density scale heights below z = 150 km (i.e., at $z \sim$ 110–130 km) [*Vadas and Liu*, 2009]. The dominant winds which filter the GWs in the lower thermosphere are semidiurnal and diurnal tides, which change on time scales of 6–12 h and vary over large spatial scales. These winds are northwestward at early times (see Figure 3).

[29] Figures 11g–11i show vertical slices of F_x at the latitude where F_x is largest: 12.3°S. The vertical extents of the body forces are $\mathcal{D}_z \sim$ 60–130 km. Figures 11j–11l show vertical slices of F_y at the longitude where F_y is largest: 52.7°W. The vertical extents of the body forces are $\mathcal{D}_z \sim$ 50–110 km. The horizontal extents of the body forces are $D_H \sim$ 1–2°, or 100–200 km.

4. Neutral and Plasma Responses From Thermospheric Body Forces From Deep Convection

[30] Horizontal body forces create secondary GWs and mean (or constant) neutral winds when molecular viscosity can be neglected [*Vadas and Fritts*, 2001]. By mean, we

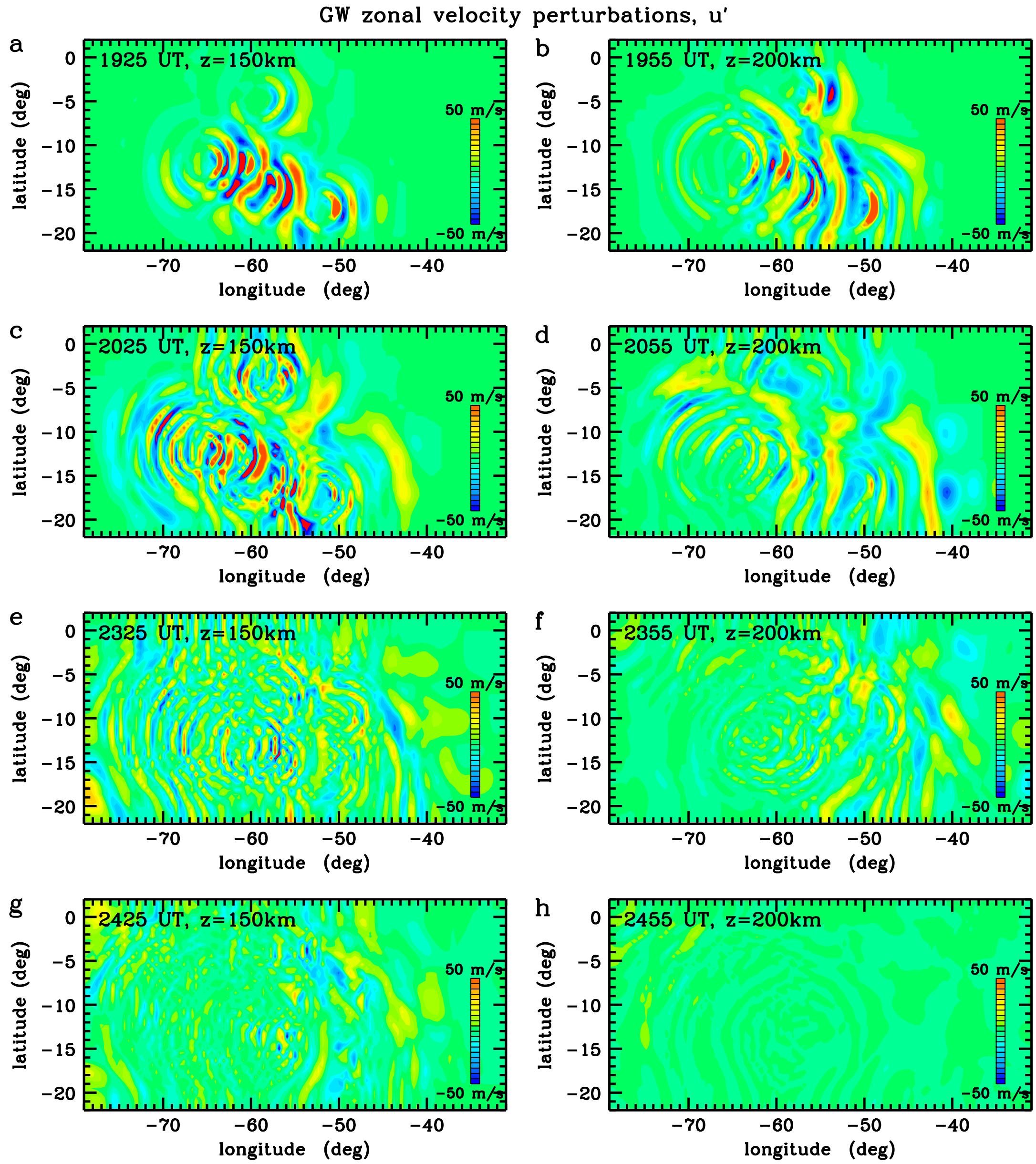

Figure 8. Reconstructed primary GW zonal velocity perturbations at the same altitudes and times as in Figure 5. The colors denote u' on a linear scale from –50 to 50 m/s. Larger wind perturbations are not shown. Note that Figures 8a–8c and 8e contain isolated locations where $|u'| > 50$ m/s.

denote that the winds are constant in time after the forcing is finished. In the thermosphere, horizontal body forces create secondary GWs and "mean" neutral winds [*Vadas and Liu*, 2009]. By "mean," we denote that the winds can be approximated as constant so long as the forcings continue (e.g., so long as deep convection occurs in a similar location). For a single body force, this mean wind forms two counter-rotating circulation cells. If the diameter of a body force is $\mathcal{D}_H$, the excited GWs will have horizontal wavelengths of $\lambda_H \sim (0.5\text{–}10) \times \mathcal{D}_H$, with a spectral tail out to larger λ_H and a peak at $\lambda_H \sim 2\mathcal{D}_H$ [*Vadas et al.*, 2003]. Because the forces in Figure 11 have spatial variability on scales of 100–200 km, we expect the secondary GWs to have horizontal wavelengths of $\lambda_H \sim$ 50–2000 km, with a peak at $\lambda_H \sim$ 200–400 km. This expectation is consistent with recent results, which found that the secondary GWs excited by deep convection had $\lambda_H \sim$ 100–2000 km and peaked at $\lambda_H \sim$ 100–300 km [*Vadas and Crowley*, 2010]. We also note that if the vertical extent of a body force or heating is $\mathcal{D}_z$, the excited (secondary) GWs will have vertical wavelengths of $|\lambda_z| \sim (1\text{–}2) \times \mathcal{D}_z$ [*Holton et al.*, 2002; *Vadas and Fritts*, 2001]. For the forces in Figure 11, we expect the excited secondary GW spectrum to peak at $|\lambda_z| \sim$ 60–250 km.

[31] We interpolate F_x and F_y from equation (2) (as a function of (x, y, z, t)) into our third model, the TIME-GCM. The TIME-GCM simulates the circulation, temperature, and compositional structures of the upper atmosphere ($\sim$ 30–500 km) and the ionosphere, and it includes the dynamical, chemical, and electrodynamical processes in that

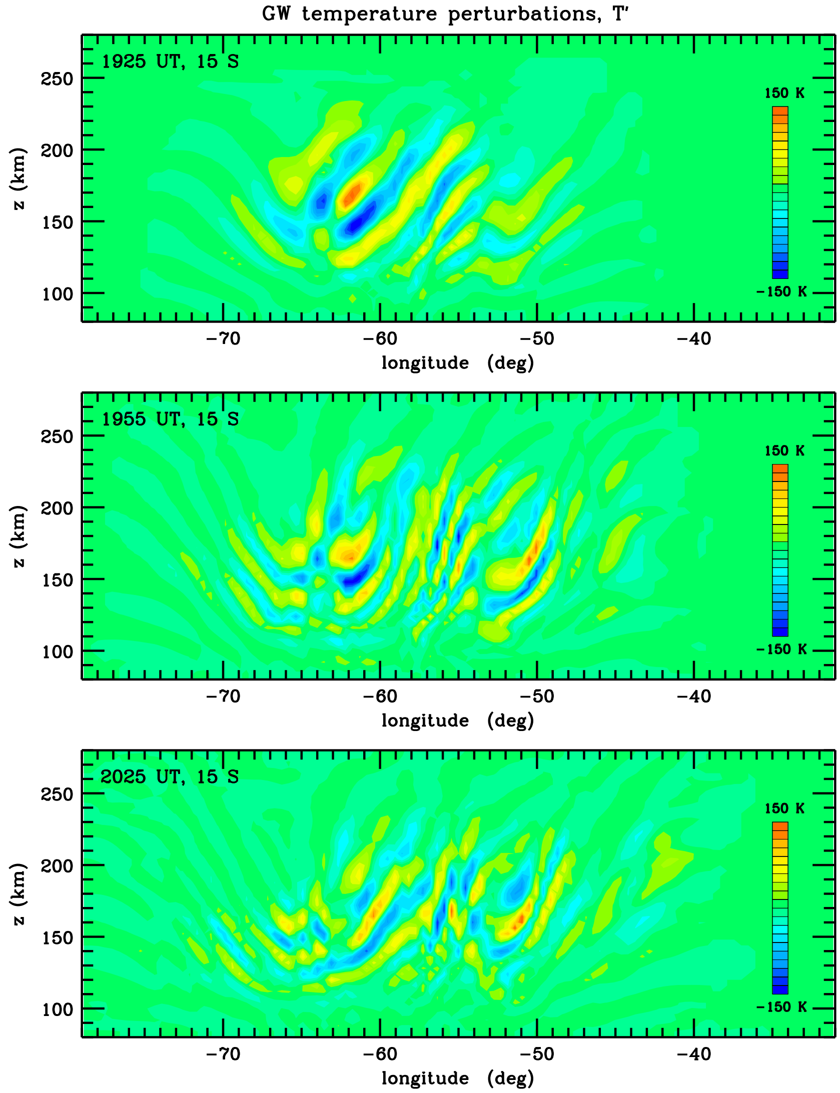

Figure 9. Reconstructed temperature perturbations of the primary GWs at 15°S. The first, second, and third rows show 19:25, 19:55, and 20:25 UT, respectively.

atmospheric region [*Roble and Ridley*, 1994]. We run the TIME-GCM at high resolution (four grids/scale height and 2.5° × 2.5°). Because the horizontal grid spacing of the TIME-GCM is 2.5°, the small-scale, horizontal variabilities of F_x and F_y are smoothed out via this interpolation. This, along with model damping, effectively causes GWs with λ_H < 2000 km to not be resolved by the TIME-GCM [*Vadas and Liu*, 2009]. Thus, only secondary GWs with λ_H > 2000 km can be resolved in this study.

[32] After running the TIME-GCM with F_x and F_y, we calculate the difference between the "perturbed" (with F_x and F_y) and "unperturbed" ($F_x = F_y = 0$) TIME-GCM solutions. We now show the neutral and plasma responses to these accelerations. All quantities in Figures 12 – 19, 21a–21c, and 22 show the perturbed minus the unperturbed TIME-GCM solutions.

4.1. Neutral Responses

[33] Figure 12 shows a satellite view (centered on Brazil) of the neutral density perturbations at z = 250 km which result from the thermospheric body forces. This is the approximate altitude of the bottomside of the F layer at sunset (see section 4.2). A few hours after deep convective overshoot (20:30–23:30 UT), there is a persistent density decrease of 8–12% over central and western Brazil. This large-scale depletion moves southward in time after deep convection ceases. There is also a corresponding persistent density increase of 7–9% over eastern Brazil and the Atlantic Ocean. This large-scale enhancement moves southeastward in time after deep convection ceases. These depletions and enhancements are due to the body forces, which accelerate the neutral fluid just below this altitude: (1) a density decrease is created near the back-half of a body force as fluid is pushed away from this region, and (2) a density increase is created near the front-half of a body force as fluid is pushed into a region containing existing fluid. The density perturbation amplitudes are smaller after 24:00 UT because the body forces are weaker then (see Figure 11). We note that the density perturbations are ≤ 4% after 26:00 UT (not shown).

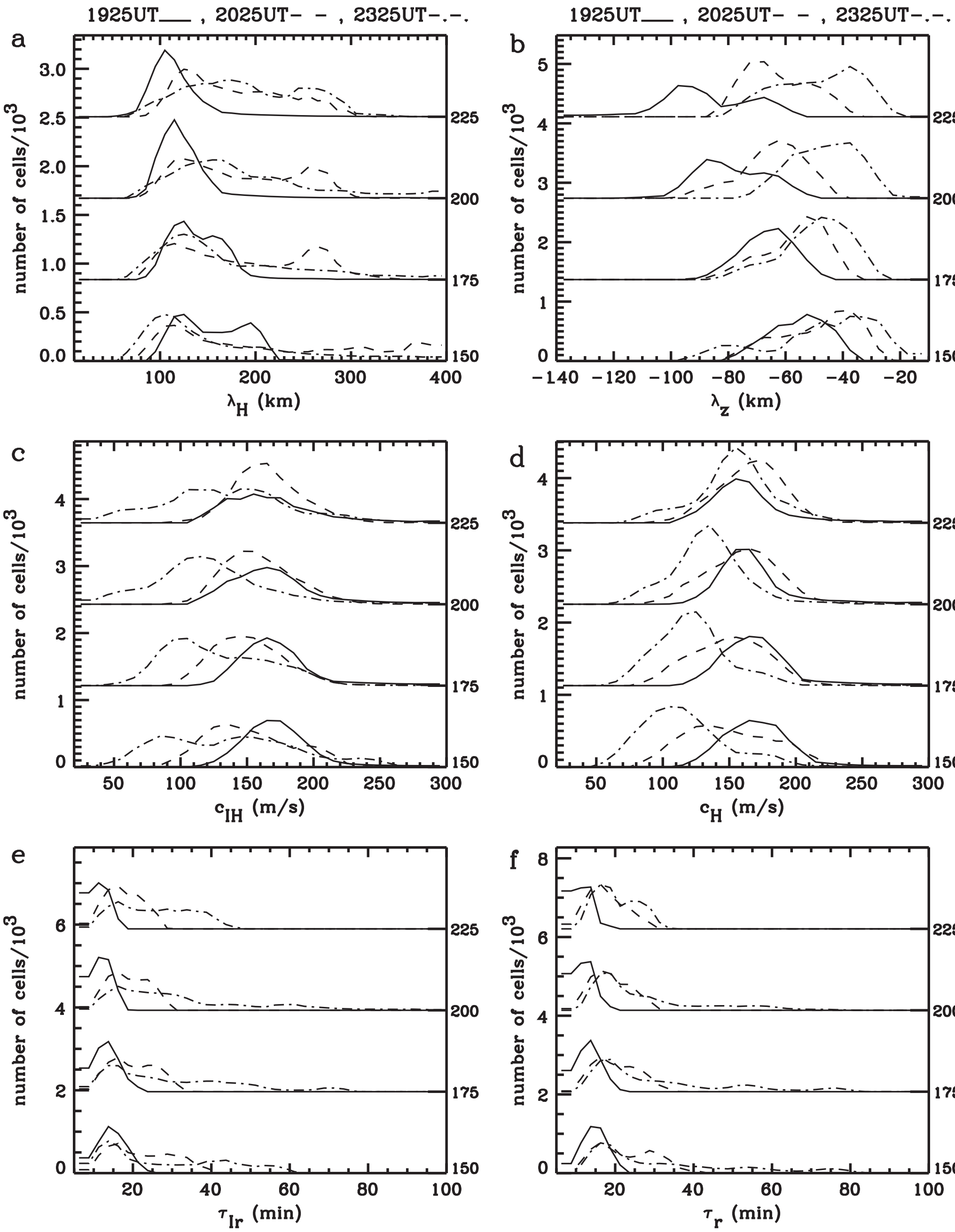

Figure 10. Distributions of the average primary GW parameters at 19:25 UT (solid), 20:25 UT (dashed), and 23:25 UT (dash-dotted). Offset results are shown at z = 150, 175, 200, and 225 km (values on right-hand y axis). (a) $\overline{\lambda_H}$. (b) $\overline{\lambda_z}$. (c) $\overline{c_{IH}}$. (d) $\overline{c_H}$. (e) $\overline{\tau_{Ir}}$. (f) $\overline{\tau_r}$.

[34] In addition to these relatively "stationary" density enhancements and depletions, large-scale secondary GWs are observed propagating southeast, east, northeast, northwest, west, and southwestward from Brazil after 21:00 UT. These GWs have horizontal phase speeds of $c_H \sim$ 500–600 m/s and $\lambda_H \sim$ 4000–5000 km. (Remember that only secondary GWs with $\lambda_H \geq$ 2000 km can be resolved by the TIME-GCM.) The secondary GWs which propagate west and southwestward have significantly smaller amplitudes than the east and southeastward GWs before 24:00 UT. After 24:00 UT, their amplitudes are comparable.

[35] The result that the westward GWs have significantly smaller amplitudes than the eastward GWs before 24:00 UT differs from previous results; *Vadas and Liu* [2009] found that the secondary GWs from a single plume have similar amplitudes in and opposite to the force direction. In fact, if the background winds are small, the secondary GWs excited by horizontal body forces have equal amplitudes in and against the force direction (for the same intrinsic frequency ω_{Ir}) in the intrinsic reference frame [*Vadas et al.*, 2003]. In *Vadas and Liu* [2009], the mean wind perturbations (or circulation cells) and secondary GWs were created at the same time. Therefore, the background winds were relatively small

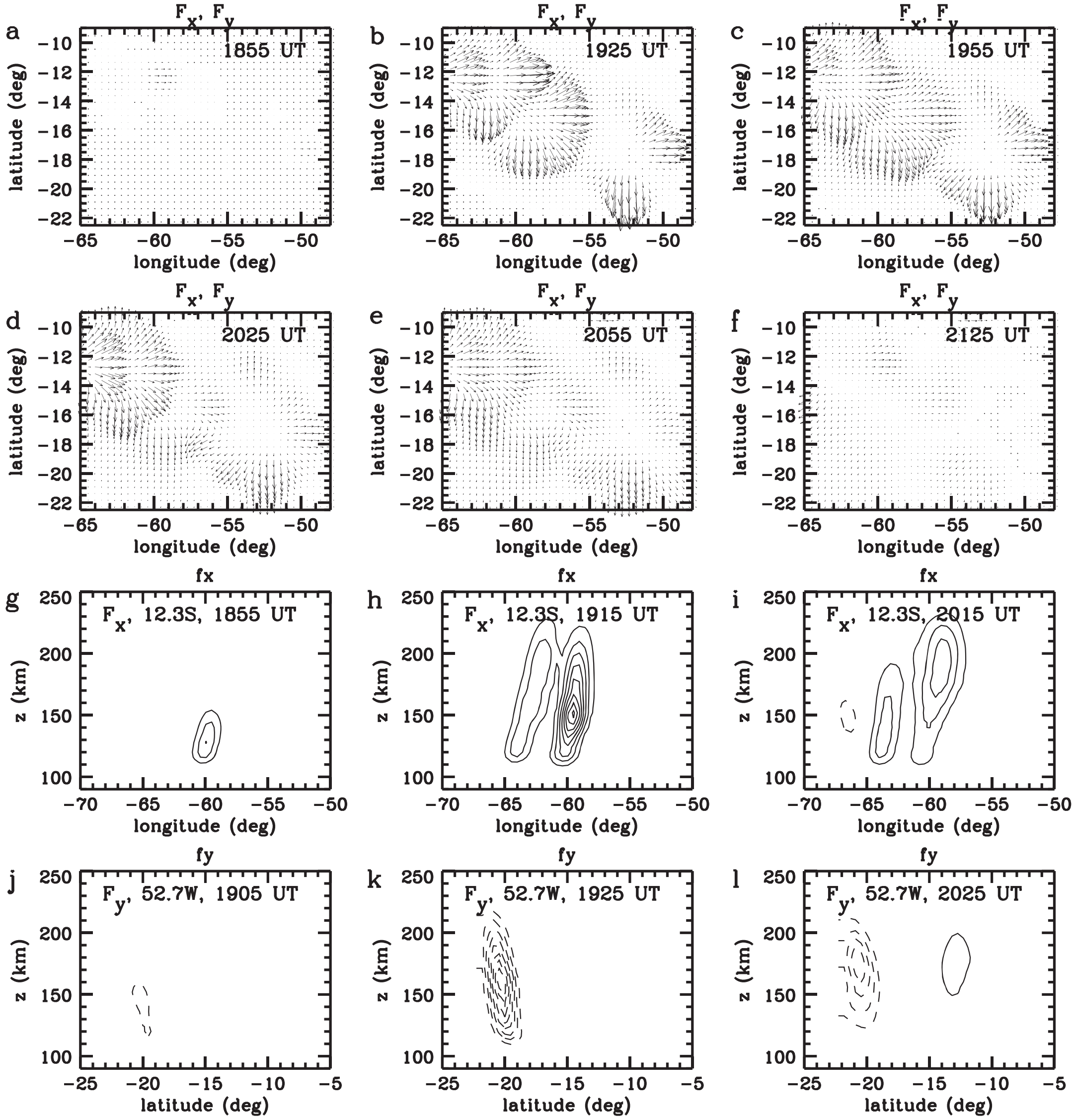

Figure 11. (a–f) Horizontal slices at z = 150 km of the horizontal accelerations, (F_x, F_y), created by the dissipation of the primary convective GWs. Times are shown every 30 min from 18:55 to 21:25 UT, with maximum accelerations of 0.1, 0.8, 0.6, 0.4, 0.3, and 0.2 m/s^2, respectively. (g–i) Vertical slices of F_x in intervals of 0.1 m/s^2 at 12.3°S and at 18:55, 19:15, and 20:15 UT, respectively. (j–l) Vertical slices of F_y in intervals of 0.1 m/s^2 at 52.7°W and at 19:05, 19:25, and 20:25 UT, respectively. For Figures 11g–11l, solid (dashed) lines indicate positive (negative) values.

at the excitation time. This is not the case prior to 24:00 UT here. Figure 13 shows the zonal wind perturbations (mean wind plus the secondary GWs) at 14°S. There are strong induced eastward mean winds at $z \sim$ 130 to 230 km and 20:00–24:00 UT, with amplitudes of $u' \sim$ 180–340 m/s and zonal extents of $\sim$ 2000–4000 km. After 24:00 UT, these induced winds decrease dramatically. There are also large induced southward and northward mean winds of $v' \sim$ 50 – 125 m/s, as shown in Figure 14. After 24:00 UT, these winds also decrease significantly. Therefore, before 24:00 UT, the secondary GWs are excited in large east, southeast, or northeastward winds created by previous thermospheric body forces. Because deep convection weakens rapidly after 23:00 UT, the induced mean winds from these forces weakens considerably after 24:00 UT (see Figures 13 and 14). As we will see in a moment, this is why the secondary GW amplitudes are asymmetric prior to 24:00 UT.

[36] We now discuss the influence of the background wind on the secondary GW amplitudes. The ground-based frequency (ω_r) of a GW is

$$\omega_r = \omega_{Ir} + kU + lV, \tag{4}$$

where U and V are the zonal and meridional background winds (which include the tides and the mean winds induced by the body forces), and (k, l, m) is the GW wavevector. We consider an eastward body force, which creates an eastward mean wind at the excitation altitude and location. For excited eastward and westward secondary GWs that have the same intrinsic frequency ω_{Ir}, the observed

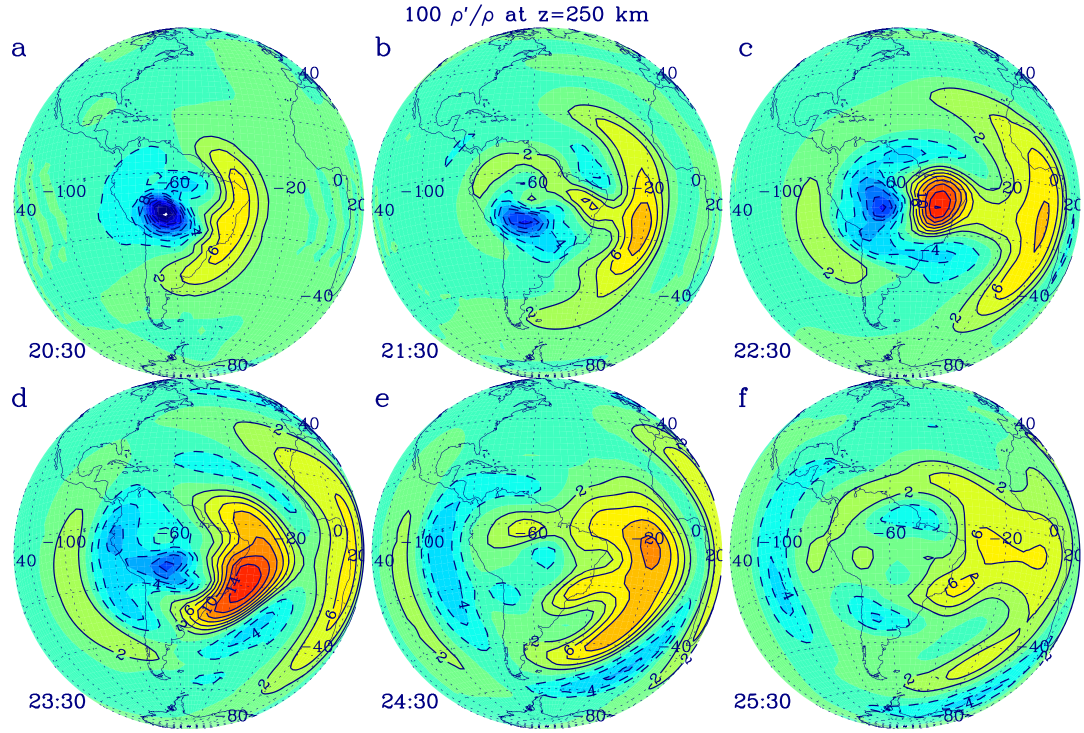

Figure 12. Neutral density perturbations at z = 250 km from the TIME-GCM. Figures 12a–12f show every hour from 20:30 to 25:30 UT. Blue (red) colors show negative (positive) values. Minimum and maximum perturbation amplitudes are (a) –21 and 8%, (b) –13 and 9%, (c) –13 and 16%, (d) –11 and 16%, (e) –6 and 11%, and (f) –5 and 7%. The latitude and longitude lines on Earth are separated by 20°.

frequencies ω_r are larger and smaller, respectively, in the forcing region for these GWs. These east and westward secondary GWs have the same initial amplitudes [*Vadas et al*., 2003]. Above the forcing region (i.e., at $z \geq 250$ km), the zonal and meridional wind induced by previous body forces, U and V, are much smaller, because all body forces have small or negligible amplitudes there. Since ω_r is constant along a GW's ray path if the winds change slowly in time [*Lighthill*, 1978], using equation (4), ω_{Ir} is therefore larger (smaller) at $z \geq 250$ km for the secondary GW propagating eastward (westward). From the dispersion relation, $|\lambda_z|$ is larger (smaller) for a GW with a larger (smaller) ω_{Ir}. Since a GW with smaller (larger) $|\lambda_z|$ and ω_{Ir} dissipates at a lower (higher) altitude [*Vadas*, 2007], the amplitudes of the eastward GWs are therefore larger than that of the westward GWs above the forcing region (i.e., at z = 250 km) prior to 24:00 UT. After 24:00 UT, the background wind at z = 150–200 km is much smaller because the body forces are weaker. This causes ω_r to be approximately equal for these same secondary GWs, causing their amplitudes to be nearly the same at z = 250 km, since they are dissipating similarly with altitude.

[37] Figures 13 and 14 also show that some secondary GWs propagate up to $z \sim 400$ km. This is particularly evident at and after 21:30 UT. These GWs have extremely large vertical wavelengths of $|\lambda_z| > 200$ km and have only slightly smaller amplitudes at z = 375 km as compared to those at z = 250 km. This confirms that large-scale GWs excited at $z \sim 180$ km with large $|\lambda_z|$ can penetrate to high altitudes in the thermosphere, as predicted by theory [*Vadas*, 2007]. Additionally, the amplitudes of the eastward and westward secondary GWs are similar after 24:00 UT, similar to Figure 12.

[38] Figure 15 shows the neutral density perturbations at z = 375 km. The mean enhancements/depletions seen in Figure 12 at z = 250 km are not apparent here. Southeast, east, northeast, northwest, west, and southwestward secondary GWs are clearly visible in these images and are in phase with the GWs at z = 250 km (Figure 12). These GWs have $c_H \sim 500$–600 m/s and $\lambda_H \sim 4000$–5000 km. Note that the amplitudes at z = 375 km are somewhat smaller than at z = 250 km because of wave dissipation.

[39] Figure 16 shows the horizontal velocity perturbations at z = 250 and 375 km prior to and after sunset. A large pair of circulation cells (oppositely directed, large-scale vortices) swirl the neutral fluid in opposite directions above the convective region at both altitudes, although the vortex takes longer to begin at z = 375 km. Persistent east and southeastward motions of $u' \sim 75$–150 m/s occur at z = 250 km where these cells converge. These perturbations last for at least 6 h at both altitudes, although they weaken somewhat by 27:30 UT (i.e., 3:30 UT the following day). We see that the induced horizontal velocity perturbations at z = 250 km are much larger than that of the primary GWs at this altitude (see Figure 7).

[40] Figure 17 shows the horizontal velocity perturbations created by the body forces at z = 250 km for all Earth in a flat projection. It is easy to see the secondary GWs with concentric-ring-like phase lines radiating in all directions away from Brazil. These secondary GWs reach Puerto Rico at 21:00–21:50 UT (17:00–18:00 local time (LT)), the Antarctic Peninsula at 21:30–22:00 UT (17:00–18:00 LT),

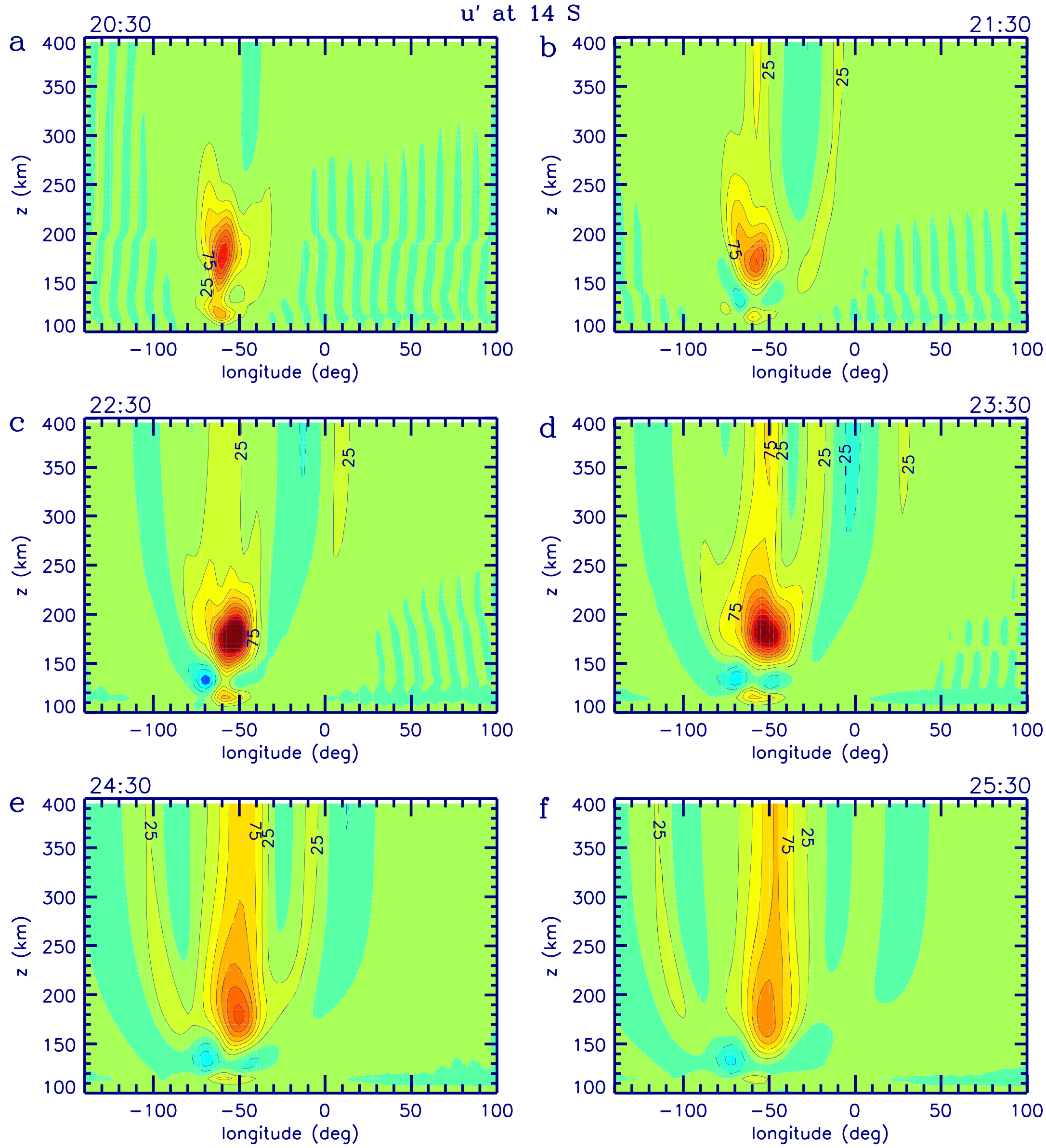

Figure 13. Neutral zonal velocity perturbations at 14°S from the TIME-GCM. Figures 13a–13f show every hour from 20:30 to 25:30 UT. Blue (red) colors show negative (positive) perturbations. Minimum and maximum perturbation amplitudes are (a) –14 and 225 m/s, (b) –50 and 180 m/s, (c) –85 and 340 m/s, (d) –70 and 280 m/s, (e) –65 and 185 m/s, and (f) –55 and 145 m/s.

eastern Africa at 21:30–22:00 UT (21:00–22:00 LT), Europe at 23:00–23:50 UT (22:00–24:00 LT), the eastern United States at 24:00 UT (19:00 LT), Moscow (Russia) at 24:00 UT (1:00–2:00 LT), Kazakhstan at 25:00 UT (4:00 LT), India at 25:00–25:30 UT (6:00–7:00 LT), western China at 26:00–26:30 UT (7:00–8:00 LT), and Thailand at 27:00 UT (9:00–10:00 LT). As the distance to Brazil increases, the GW amplitudes decrease due to geometric attenuation. Although it appears that the secondary GWs are propagating horizontally away from Brazil, they are not; each GW propagates vertically as well, albeit slowly. The effect occurs because the body forces excite a coherent spectrum of secondary GWs. Those GWs which reach India at z = 250 km have somewhat smaller angles with respect to the horizontal than those which reach Africa at z = 250 km. Apart from wind effects, a smaller angle translates into a smaller frequency or larger period [*Hines*, 1967]. Since those GWs with smaller frequencies tend to have smaller vertical wavelengths, they take longer to reach this altitude. This is why the waves appear to radiate outward from Brazil at this fixed altitude.

[41] Figure 18 shows the zonal velocity, meridional velocity, and temperature perturbations at z = 250 km at varying locations around Earth. Perturbations of 10–20 m/s and 5–15 K are created at South Pole Station (Antarctica), Europe, and the USA. Relatively large velocity perturbations of 20–30 m/s occur at Cape Town (South Africa) and Rothera Research Station (Antarctica). Smaller perturbations (5–15 m/s and 5–10 K) are created in Moscow (Russia) and New Delhi (India). Very small perturbations (5–10 m/s and 2–5 K) are created in Jakarta

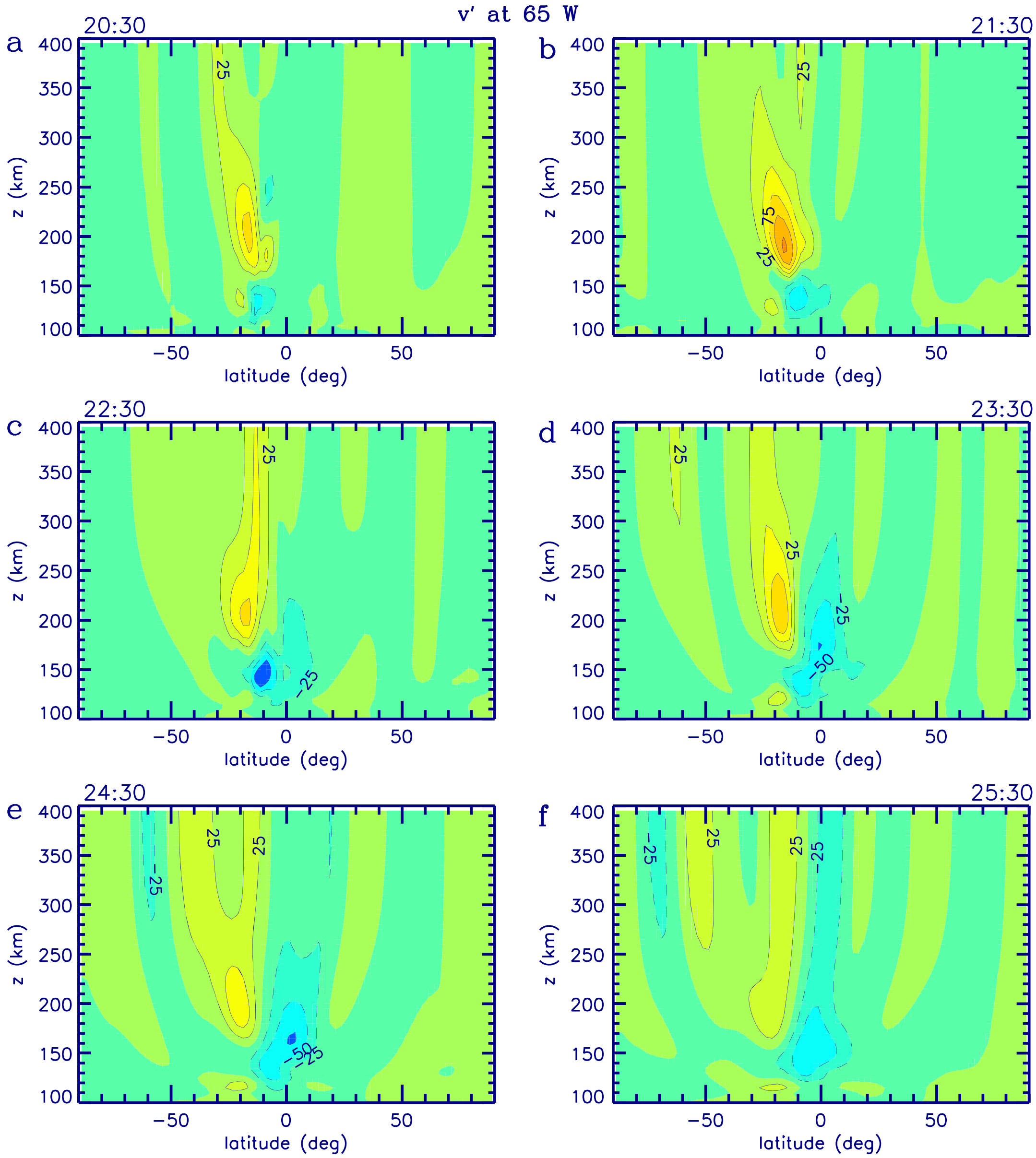

Figure 14. Neutral meridional velocity perturbations at 65°W from the TIME-GCM. Figures14a–14f show every hour from 20:30 to 25:30 UT. Blue (red) colors show negative (positive) perturbations. Minimum and maximum perturbation amplitudes are (a) –60 and 90 m/s, (b) –70 and 130 m/s, (c) –100 and 80 m/s, (d) –75 and 100 m/s, (e) –75 and 70 m/s, and (f) –75 and 40 m/s.

(Indonesia). Thus, large-scale secondary GWs created in a two-step process (described herein) by tropical storms in the Amazon region of Brazil can, in principle, be detected in Indonesia ($\sim$ 20,000 km away). This is quite remarkable, given the small-scale nature of the convective plumes. We note that GWs with amplitudes of 20–30 m/s can easily be detected with the new Fabry Perot systems [*Nicolls et al.*, 2012]. At most locations shown in Figure 18, the perturbations within the wave packet are quasi-sinusoidal; this is because the temporal variability of the source, 0.5–4 h, is imposed on the GWs, thereby creating wave packets which disperse in time and space. In many (but not all) cases, the shape of the temperature perturbations mimic the velocity perturbations but with an offset that depends on the GW wavelength and background parameters [*Vadas and Nicolls*, 2012]. Note that the vertical wind perturbations associated with these large-scale waves are quite small ($\ll$ 1 m/s).

[42] Figure 19 shows the temperature perturbations of the secondary GWs at z = 250 km as these waves propagate across the Antarctic continent. They reach the tip of the Antarctic Peninsula at 21:00 UT, the continent at 22:00 UT, and the South Pole at 23:00 UT. The wave packet consists of two to three wave cycles (see also Figure 18). The GWs have periods of $\tau_r \sim$ 2.5–3 h, $\lambda_H \sim$ 5000–5500 km and phase speeds of $c_H \sim$ 450–600 m/s. Note that these GWs reach the Antarctic Peninsula $\sim$ 2–2.5 h after deep convection in Brazil.

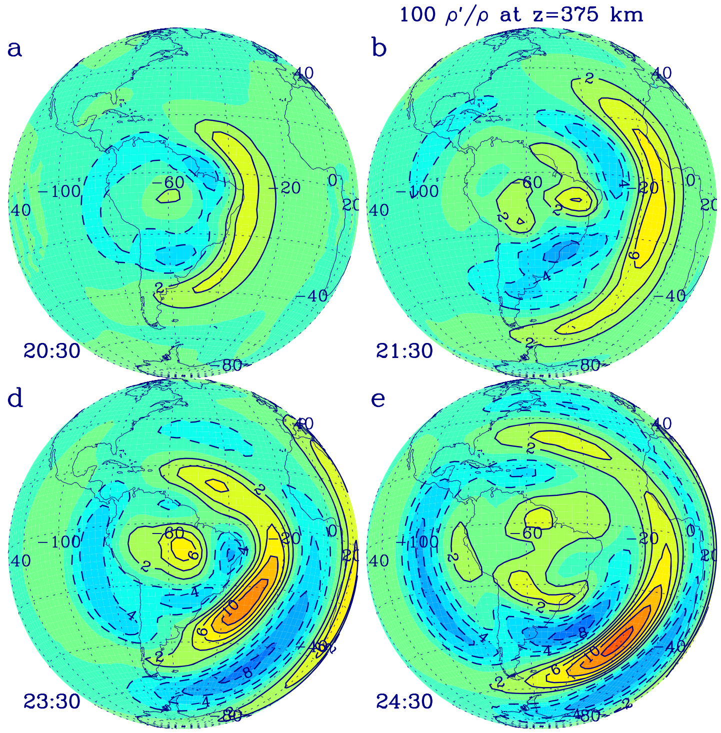

Figure 15. Same as Figure 12, but at $z = 375$ km. Minimum and maximum density perturbation amplitudes are (a) –6 and 5%, (b) –7 and 8%, (c) –8 and 9%, (d) –8 and 12%, (e) –9 and 13%, and (f) –8 and 9%.

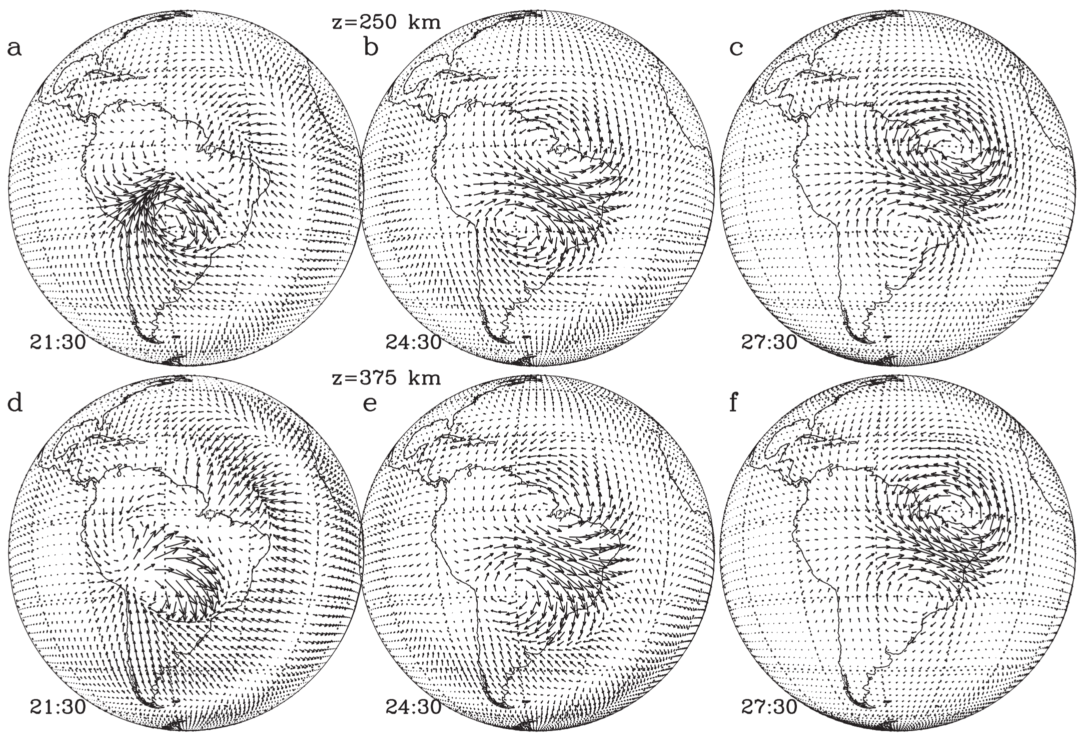

Figure 16. Horizontal velocity perturbations at $z = 250$ km (in Figures 16a–16c) and $z = 375$ km (in Figures 16d–16f) from the TIME-GCM. (a, d) 21:30 UT. (b, e) 24:30 UT. (c, f) 27:30 UT. Maximum perturbation amplitudes are 70 m/s (in Figure 16a), 150 m/s (in Figure 16b), 105 m/s (in Figure 16c), 65 m/s (in Figure 16d), 125 m/s (in Figure 16e), and 105 m/s (in Figure 16f). The latitude and longitude lines on Earth are separated by 20°.

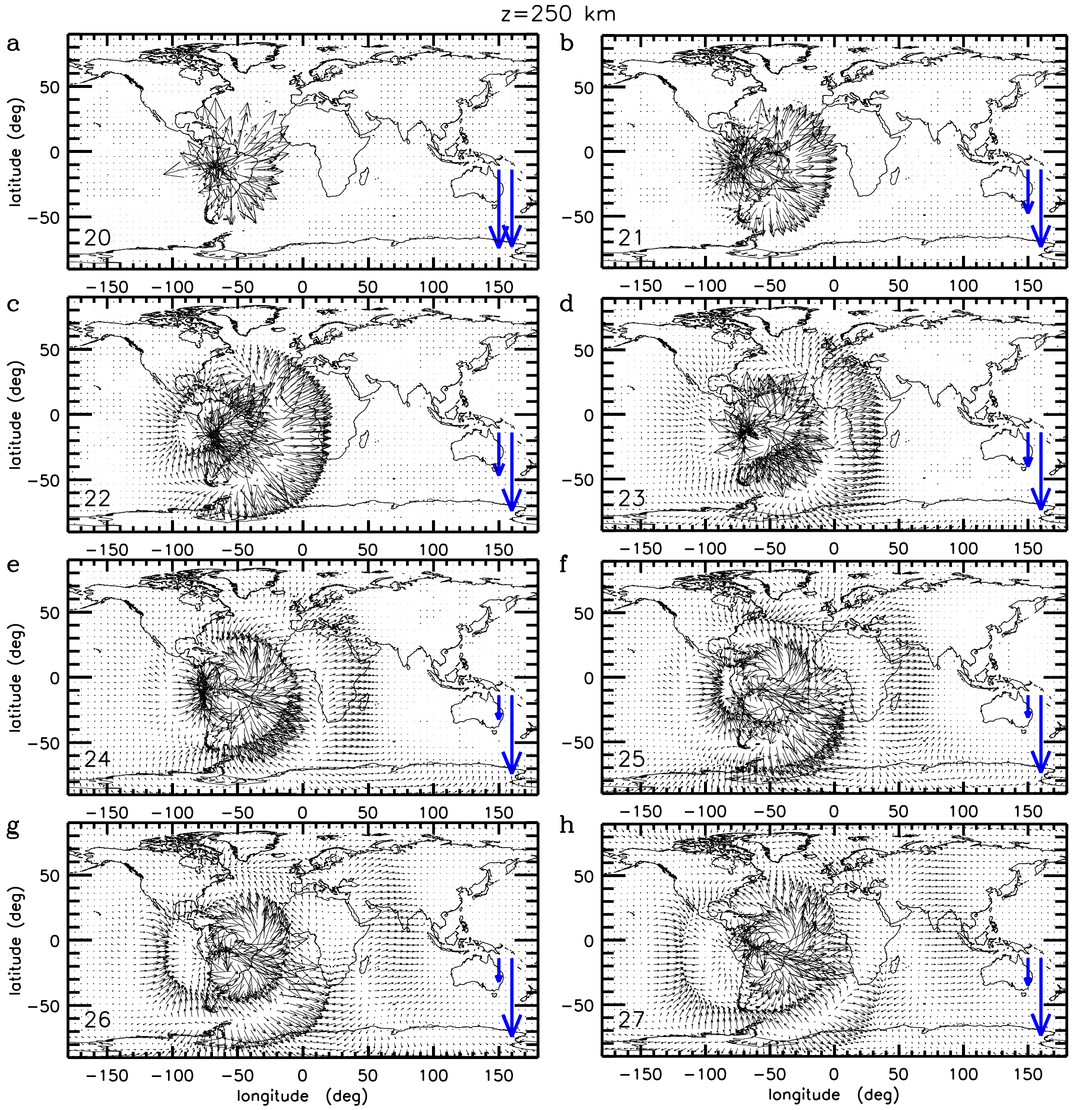

Figure 17. (a–h) Horizontal velocity perturbations from the TIME-GCM at $z = 250$ km every hour from 20:00 to 27:00 UT. Maximum perturbation amplitudes in Figures 17a–17h are 40, 75, 75, 90, 140, 145, 135, and 115 m/s, respectively. The vector lengths are exaggerated here as compared to Figure 16 in order to more easily discern the smaller-amplitude secondary GWs propagating large distances from Brazil. The blue arrows are the same as in Figure 6.

4.2. Plasma Responses

[43] The ionosphere is also significantly affected by the thermospheric body forces created by the dissipation of primary GWs. We now discuss the plasma responses to these forces.

[44] Figure 20 shows electron density, N_e, profiles at various times near the center of the body forces. For both unperturbed and perturbed solutions, the F peak is located at $z \sim 400$ km at 20:00 UT (a few hours before sunset) and decreases to $z \sim 300$ km by 28:00 UT. The electron density at the F peak decreases rapidly after sunset due to the lack of photoionization. Note that the bottomside of the F layer is $z \sim 240$–250 km at sunset.

[45] Figures 21a–21c show the perturbed minus the unperturbed values of the $F2$ peak plasma frequency (f_oF2'), the total electron content (TEC′), and the altitude of the $F2$ peak (h_mF2'). Here, TEC is calculated up to the model top, which will neglect contributions from above this altitude. Figure 21d shows the altitude of the $F2$ peak for the perturbed solution, h_mF2. Here, the plasma frequency is derived from the refractive index of electromagnetic waves in partially ionized media. A full treatment can be found in *Rishbeth and Garriott* [1969]. We use the expression for the so-called "ordinary" wave, typical for ionosonde measurements:

$$f_oF2 = 9 \times 10^{-6} \sqrt{N_mF2}, \tag{5}$$

where f_oF2 is in megahertz and N_e is in inverse cubic meters. Here, N_mF2 is the electron density N_e at the peak of the $F2$ layer. The TEC is the vertical integration of N_e. Note that for

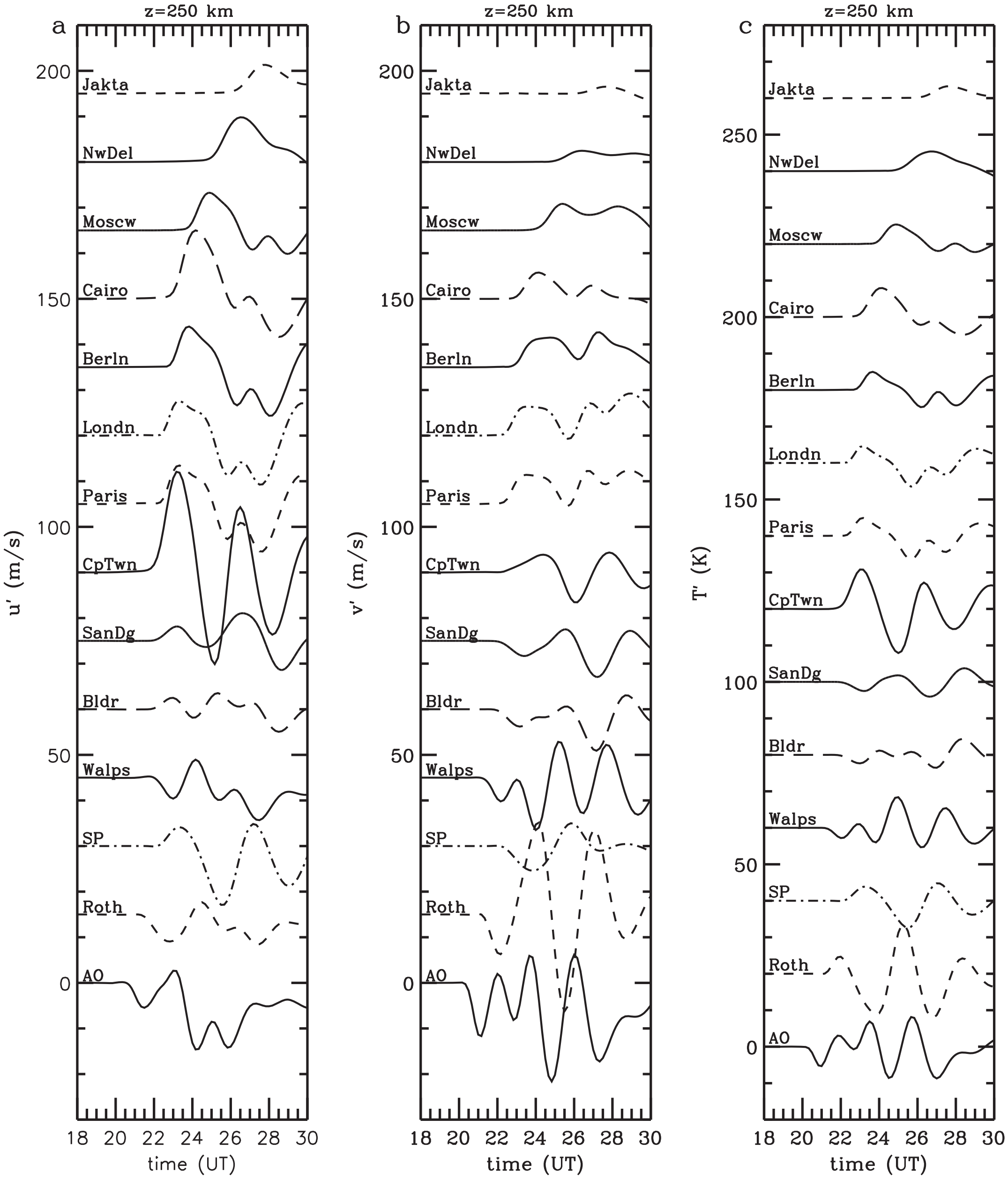

Figure 18. (a) Zonal velocity, (b) meridional velocity, and (c) temperature perturbations at z = 250 km from the TIME-GCM. Lower to upper plots indicate Arecibo Observatory (Puerto Rico), Rothera Station (Antarctic Peninsula), South Pole (Antarctica), Wallops Island, VA (USA), Boulder, CO (USA), San Diego, CA (USA), Cape Town (South Africa), Paris (France), London (UK), Berlin (Germany), Cairo (Egypt), Moscow (Russia), New Delhi (India), and Jakarta (Indonesia). Plots in Figures 18a and 18b are offset by 15 m/s, and plots in Figure 18c are offset by 20 K.

z > 200 km, the ions are composed mainly of O^+. We do not show the region south of 60°S in Figure 21 in order to avoid seeing the effects of nighttime auroral precipitation and strong transport by electric fields.

[46] We see that the plasma response to the thermospheric body forces is large. The induced perturbations are 0.2–1.0 MHz in plasma frequency, 0.4–1.5 TECU (total electron content unit, 1 TECU = 10^{16} el m^{-2}) in TEC, and 5–50 km in h_mF2. These perturbations span the width of the South American continent. Increases in TEC are generally correlated with increases in f_oF2, because increases in N_mF2 (through equation (5)) results in larger integrated column densities (if N_e can be considered negligible above the model top). Large, persistent TEC perturbations are present above the body forces. Note that the ionospheric chemistry significantly reduces the plasma response during the daytime. Also, the h_mF2' perturbations are generally anticorrelated with the f_oF2' and TEC′ perturbations. This indicates that field-aligned transport may be the dominant mechanism, not chemistry (i.e., $[e] + [O^+]$ recombination).

[47] By comparing the general features in Figures 21 and 16, it is seen that the neutral motion in the magnetic

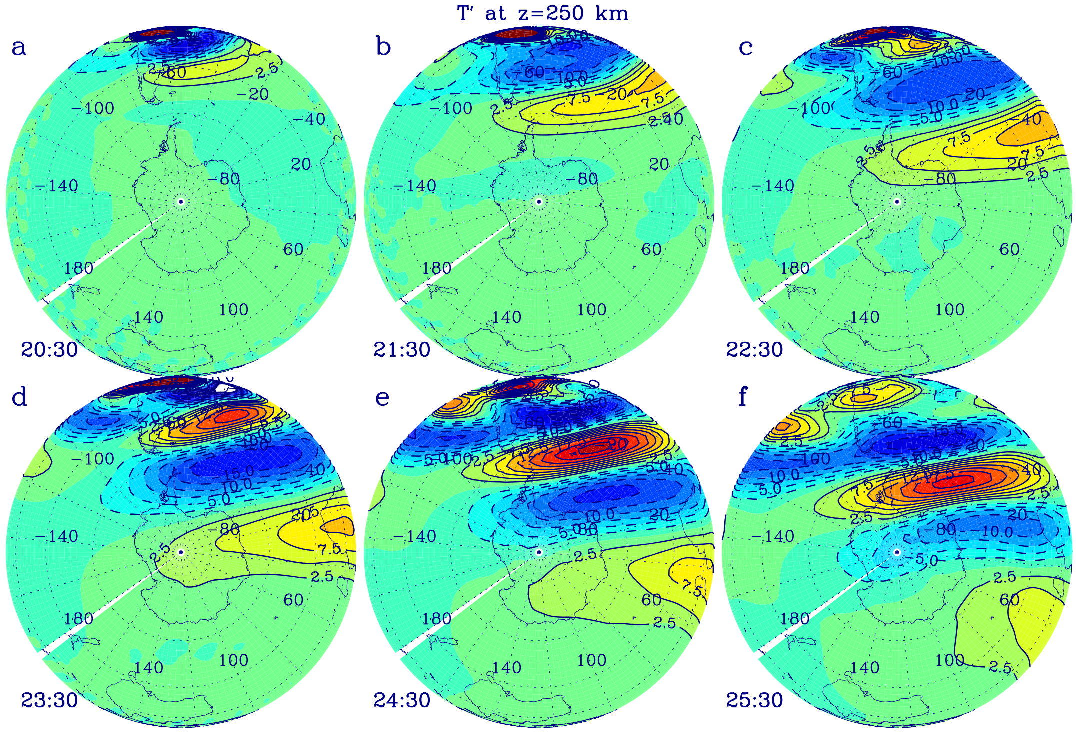

Figure 19. Neutral temperature perturbations (in K) at $z = 250$ km from the TIME-GCM. Figures 19a–19f show every hour from 20:30 to 25:30 UT. Blue (red) colors show negative (positive) values. Maximum perturbation amplitudes are (a) 55 K, (b) 55 K, (c) 35 K, (d) 55 K, (e) 25 K, and (f) 20 K.

equatorward direction pushes the plasma to higher altitudes, resulting in smaller N_mF2, f_oF2 and TEC, while the neutral motion in the magnetic poleward direction pushes the plasma to lower altitudes, resulting in larger N_mF2, f_oF2 and TEC. For example, this can be seen in Figure 16e at 24:30 UT and $z = 375$ km over the South American continent, which shows equatorward flow at 0°–10° magnetic north west of 55°W, poleward flow at 0°–20° magnetic south east of 60°W, and equatorward flow at 20°–30° magnetic south. This corresponds to a decrease, increase, and decrease of the TEC, respectively, in Figure 21b. (Note that from Figure 21d, the height of the $F2$ peak is 360–400 km at $\sim$22:00–25:00 UT in the northern part of South America.) Thus, N_mF2, f_oF2 and TEC perturbations are significantly correlated with the induced neutral wind perturbations. This is because field-aligned transport was determined to be the dominant mechanism in *Liu and Vadas* [2013].

[48] As noted in *Vadas and Liu* [2009], the TEC perturbations above the body forces are long-lasting. This is likely because the induced neutral wind at $z \sim 375$ km is long-lasting, retaining large values up to at least 27:30 UT (see Figures 13, 14 and 16d–16f). It is noteworthy that at this higher altitude, the induced neutral wind lasts much longer than the wind induced at the location of the body force (i.e., at $z \sim 150$–200 km). This is likely because of the secondary GWs, because the circulation cell dissipates within a few hours after the body forces cease [*Vadas and Liu*, 2009].

[49] Large-scale traveling ionospheric disturbances (LSTIDs) induced by the secondary GWs are also observed propagating away from the body forces. Note the concentric ring structure in the Atlantic Ocean at 22:30 and 22:40 UT. Because field-aligned transport plays the dominant role in perturbing plasma density [*Liu and Vadas*, 2013], the largest field-aligned components will occur when the

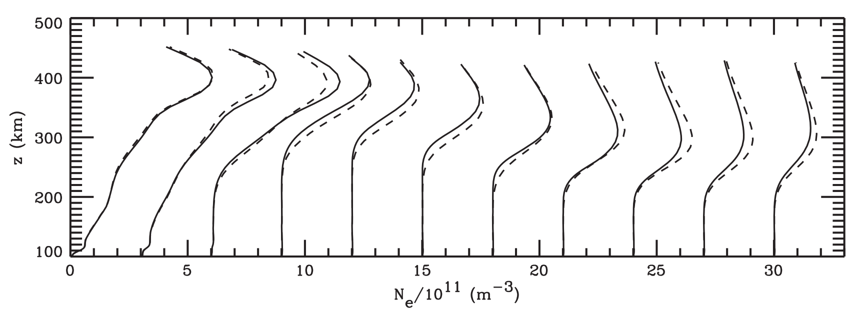

Figure 20. N_e profiles at 55°W and 11.25°S every hour from 20:00 to 30:00 UT from the TIME-GCM. The profiles are offset by $3 \times 10^{11} m^{-3}$. The solid (dashed) lines show the unperturbed (perturbed) TIME-GCM solution.

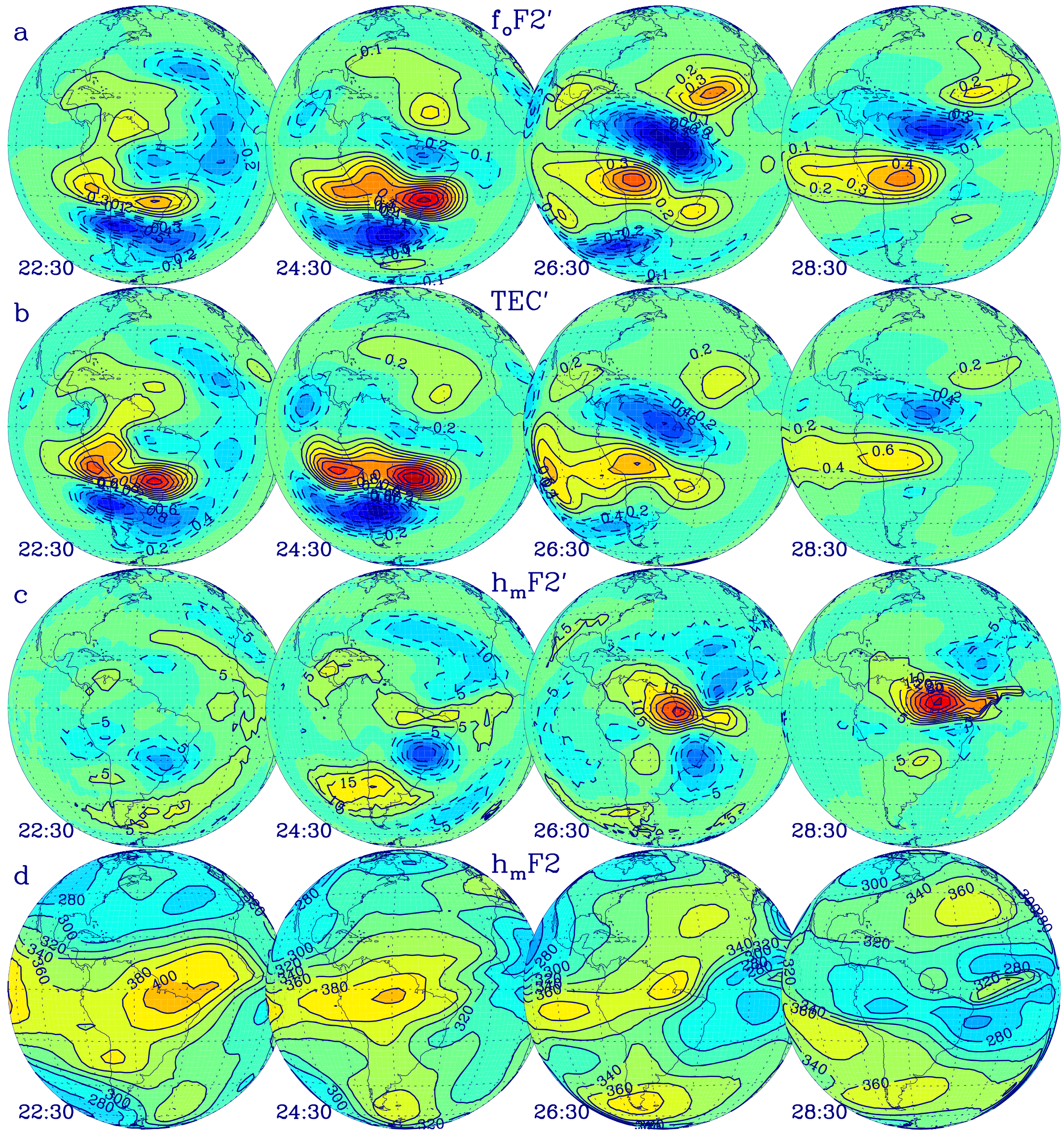

Figure 21. (a) F2 plasma frequency perturbation (f_oF2' in megahertz), (b) TEC perturbation (in TECU), (c) h_mF2 perturbation (in km), and (d) h_mF2 altitude (in km). These quantities are calculated from the TIME-GCM solutions, and are shown every 2 h from 22:30 to 28:30 UT, as labeled. 1 TECU = 10^{16} electrons m^{-2}. The contour lines are separated by 0.1 MHz, 0.2 TECU, 5 km, and 20 km in Figures 21a–21d, respectively. Note that Figures 21a–21c show the perturbed minus the unperturbed TIME-GCM solutions, while Figure 21d shows only the perturbed TIME-GCM solution.

secondary GWs have the largest geomagnetic south or north components in their wind perturbations. For high-frequency GWs, the horizontal velocity vectors are orientated along the propagation direction [*Fritts and Alexander*, 2003]; low frequency waves, however, are significantly affected by the Coriolis force, which causes horizontal rotation of the wind vector. These preceding arguments explain the general result that the phase lines of the largest TEC, h_mF2, and f_oF2 perturbations propagate geomagnetic southward and northward near Brazil (where the secondary GW frequencies are high). Further from Brazil, however, the secondary GWs have lower frequencies; in these cases, the neutral horizontal velocity vectors must be examined.

[50] From Figure 17, the south and southwestward secondary GWs have large horizontal velocity amplitudes at 26:00 UT (tip of South America). These waves are moving along the magnetic field direction and create large negative $f_oF2' \sim 0.3$–0.5 MHz and TEC$' \sim 0.3$–0.6 TECU perturbations, and positive $h_mF2' \sim$5–10 km perturbations (15–20%, 30%, and 2%, respectively) in Figures 21a – 21c. Additionally, the northeastward secondary GWs have large horizontal velocity perturbations at 22:00 UT (eastern edge of the northern African continent). A blowup of Figure 17c (not shown) reveals that these longer-period GWs have northward perturbation velocities at this location, which is parallel to the magnetic field lines. This results in relatively large-amplitude LSTIDs of negative $f_oF2' \sim 0.2$–0.3 MHz and TEC$' \sim 0.2$–0.3 TECU perturbations and positive $h_mF2' \sim$5 km perturbations (5–10%, 10–15%, and 1–2%, respectively) in Figures 21a–21c.

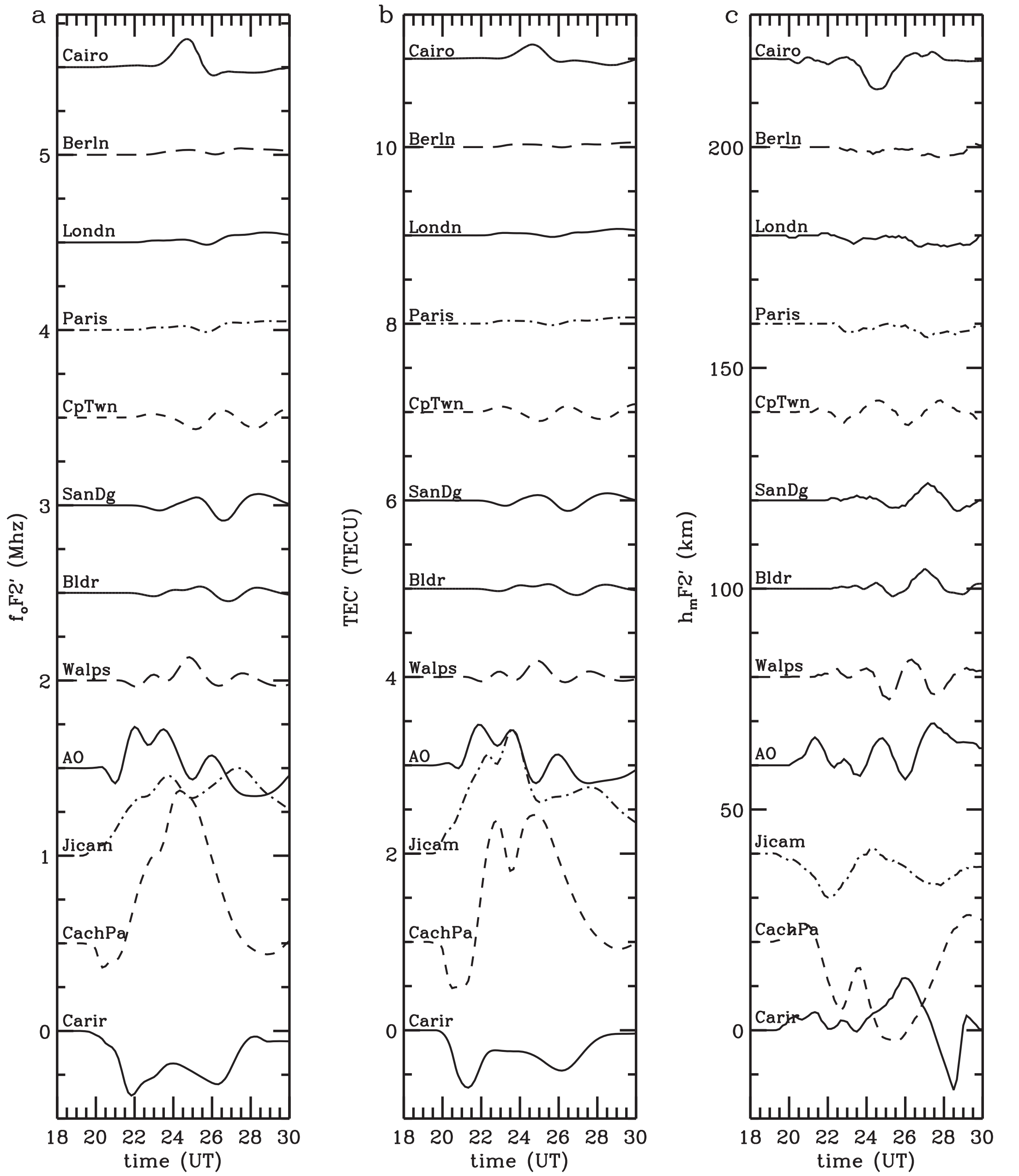

Figure 22. (a) f_oF2', (b) TEC′, and (c) h_mF2' from the TIME-GCM. Lower to upper plots indicate Cariri (Brazil), Cachoeira Paulista (Brazil), Jicamarca Radio Observatory (Peru), Arecibo Observatory (Puerto Rico), Wallops Island, VA (USA), Boulder, CO (USA), San Diego, CA (USA), Cape Town (South Africa), Paris (France), London (UK), Berlin (Germany), and Cairo (Egypt). Plots in Figures 22a, 22b, and 22c are offset by 0.5 MHz, 1.0 TECU, and 20 km, respectively.

[51] However, the following is an example of a GW which induces an LSTID with small f_oF2' and TEC′ perturbations but with large h_mF2' perturbations. The southeastward secondary GWs at 24:00 UT have large-amplitude horizontal velocity perturbations (southeast of the south American continent in Figure 17), which correspond to small positive $f_oF2' \sim 0.05$ MHz and TEC′ $\sim$ 0.1 TECU perturbations and large negative h_mF2' $\sim$5–10 km perturbations in Figures 21a–21c. At this location, the propagation direction is approximately parallel to the magnetic field lines. This indicates that the relationship between h_mF2' and N_mF2' is complex, and more detailed analysis is needed.

[52] Figure 22 shows the perturbed minus the unperturbed solutions, f_oF2', TEC′, and h_mF2', at varying locations around Earth. These locations are the same as in Figure 18, except that here we show the responses at Cariri (Brazil), Cachoeira Paulista (Brazil), and Jicamarca Radio Observatory (Peru). We do not show the responses at Moscow, New Delhi, and Jakarta because they are quite small. At later times, these small amplitudes may be due to dayside photochemistry when ion densities are large, which significantly reduces the observed amplitudes of LSTIDs [*Hajkowicz*, 1990]. Although the neutral response at Cape Town is large and the neutral responses at Paris, London, and Berlin are

reasonably large (see Figure 18), the plasma responses at these locations are small. The responses at Cariri, Cachoeira Paulista, and Jicamarca Radio Observatory are quite large, with amplitudes of $f_oF2' \sim 0.4$–1.0 MHz, TEC$' \sim 0.6$–1.5 TECU, and $h_mF2' \sim 10$–20 km. Note that the perturbations are nonsinusoidal in the vicinity of the forcing but are sinusoidal or quasi-sinusoidal (wave-like) far from the forcing (e.g., Cape Town), where secondary GWs are directly creating the LSTIDs.

5. Conclusions

[53] In this paper, we modeled the primary GWs excited by 6 h of deep convection in Brazil on the evening of 01 October 2005. We then ray traced these GWs (with their phases) into the thermosphere and reconstructed the GW fields there. We found that large-amplitude, neutral perturbations are created by the primary GWs at $z < 300$ km. For example, the primary GWs have horizontal wind perturbations of up to several hundred meters per second at $z = 150$ km, temperature perturbations of up to several hundred K, and density perturbations of up to 25%. In addition, we found that these primary GWs have $\lambda_H \sim 100$–300 km, $c_H \sim 100$–250 m/s, and $\tau_r \sim 10$–40 min. We then calculated the body forces that these primary GWs created in the thermosphere when and where they dissipated. These forces had amplitudes of 0.2–1.0m/s^2, spatial variability of $\sim$ several hundred kilometers, and temporal variability of < 30 min.

[54] Next, we interpolated these spatially and temporally varying forces into the high-resolution TIME-GCM in order to determine the large-scale neutral and plasma responses which resulted. We found that two large counter-rotating circulation cells were created over Brazil, with amplitudes of $\sim$ 50–340 m/s. The largest amplitudes occurred where these cells converged. The direction of the wind at this convergence is the general direction of the body forces, which depends sensitively on the background winds in the lower thermosphere. These winds are made up of diurnal and semidiurnal tides, planetary waves, etc. Note that because the TIME-GCM is a climatological model, it may not be able to accurately predict the winds in the lower thermosphere. Although the body force directions are somewhat uncertain (due to the uncertainty in the winds that evening), the general response (i.e., the circulation cells and secondary GWs) are a robust consequence of thermospheric body forces.

[55] Additionally, we found that large density perturbations of up to $\rho'/\overline{\rho} \sim 25\%$ and 15% were created at $z = 250$ and 375 km, respectively. Part of these were mean perturbations resulting directly from the forcings; the other parts were created by the secondary GWs excited by the forcings. Depending on the distance from Brazil, the excited secondary GWs had velocity amplitudes of $u_H \sim 10$–50 m/s and $\rho'/\overline{\rho} \sim 10$–15% at $z = 375$ km; their amplitudes decreased with distance due to geometric attenuation. They also had $c_H \sim 500$–600 m/s and $\lambda_H \sim 4000$–5000 km. These modeled GWs propagated rapidly across the Antarctic, Africa, Europe, and Asia within 2–10 h, depending on the distance from Brazil. It is important to note that our (TIME-GCM) model could not resolve secondary GWs with $\lambda_H < 2000$ km due to the 250 km grid spacing and small-scale dissipation in the TIME-GCM. Since *Vadas and Crowley* [2010] found that the secondary GW spectrum from deep convection peaks at medium scales of $\lambda_H \sim 200$–500 km, it is likely that only the large-scale tail of the secondary GW spectrum is resolved in this study. Therefore, future model simulations with higher horizontal resolution are expected to reveal excited secondary GWs that peak at medium scales.

[56] Large positive and negative f_oF2, TEC, and h_mF2 perturbations were created in South America above the body forces. These perturbation had amplitudes of $f_oF2 \sim 0.2$–1.0 MHz, TEC$' \sim 0.4$–1.5 TECU, and $h_mF2 \sim$ 5–50 km. Increases in TEC were generally correlated with increases in f_oF2. These perturbations were caused, in large part, by field-aligned transport from the induced neutral wind perturbations [*Liu and Vadas*, 2013]. These perturbations lasted for at least 6 h, although their amplitudes began to decrease slowly after 2–3 h. This is likely because the induced neutral wind at $z \sim 375$ km was long-lasting. Additionally, we found that LSTIDs were induced by the propagating secondary GWs. These modeled LSTIDs followed these GWs globally, although with smaller amplitudes far from the South American continent. These LSTIDs had amplitudes of $f_oF2' \sim 0.2$–0.5 MHz, TEC$' \sim 0.2$–0.6 TECU, and $h_mF2' \sim$5–10 km.

[57] It is remarkable that convective plumes in the tropics (with diameters of 5–20 km and temporal variability of 5–15 min) create large-scale, fast GWs in the thermosphere with spatial scales of 2000–6000 km, temporal scales of several hours, and phase speeds much larger than the sound speed in the lower atmosphere. While small and medium-scale primary GWs from convective plumes can only propagate several hundred to several thousand kilometers, these large-scale secondary GWs can easily propagate tens of thousands of kilometers from these convective plumes. This two-step process highlights the complex, global coupling expected to occur between different regions of the neutral atmosphere on different spatial and temporal scales. Because deep convection is an everyday occurrence all over the world, this modeling study suggests that GWs from deep convection play an important role in contributing variability to the thermosphere and ionosphere worldwide. Future studies will look for evidence of this coupling process using TEC and other data.

[58] **Acknowledgments.** We would like to thank Pete Stamus for the convective plume/cluster parameters, Fernando Sao Sabbas for the GOES-12 satellite images, Ben Foster for implementing the body forces into the TIME-GCM, and Art Richmond for guidance on interpreting the TIME-GCM plasma data. We would also like to thank Giovanni Occhipinti and an anonymous reviewer for reviewing this paper. S.L.V. was supported by NASA contracts NNH07CC81C and NNH10CC98C. H.L.L. was supported in part by NASA contracts NNH07CC81C and NNH10CC98C. The National Center for Atmospheric Research is sponsored by the National Science Foundation.

[59] Robert Lysak thanks the reviewers for their assistance in evaluating this paper.

References

Alexander, M. J., J. R. Holton, and D. R. Durran (1995), The gravity wave response above deep convection in a squall line simulation, *J. Atmos. Sci.*, *52*(12), 2212–2226, doi:10.1175/1520-0469.

Andrews, D. G., J. R. Holton, and C. B. Leovy (1987), *Middle Atmosphere Dynamics*, Academic Press, Florida.

Bauer, S. J. (1958), An apparent ionospheric response to the passage of hurricanes, *J. Geophys. Res.*, *63*, 265–269.

Becker, E. (2004), Direct heating rates associated with gravity wave saturation, *J. Atmos. Terr. Phys.*, *66*, 683–696.

Beres, J. H. (2004), Gravity wave generation by a three-dimensional thermal forcing, *J. Atmos. Sci.*, *61*, 1805–1815.

Bishop, R., N. Aponte, G. D. Earle, M. Sulzer, M. Larsen, and G. Peng (2006), Arecibo observations of ionospheric perturbations associated with the passage of tropical storm Odette, *J. Geophys. Res.*, *111*, A11320, doi:10.1029/2006JA011668.

Bretherton, F. P. (1969), On the mean motion induced by internal gravity waves, *J. Fluid Mech.*, *36*, 785–803.

Choi, H.-J., H.-Y. Chun, and I.-S. Song (2007), Characteristics and momentum flux spectrum of convectively forced internal gravity waves in ensemble numerical simulations, *J. Atmos. Sci.*, *64*, 3723–3734.

Crowley, G, T. B. Jones, and J. R. Dudeney (1987), Comparison of short period TID morphologies in Antarctica during geomagnetically quiet and active intervals, *J. Atmos. Terres. Phys.*, *49*, 1155–1162.

Crowley, G., and F. S. Rodrigues (2012), Characteristics of traveling ionospheric disturbances observed by the TIDDBIT sounder, *Radio Sci.*, *47*, RS0L22, doi:10.1029/2011RS004959.

Djuth, F. T., M. P. Sulzer, S. A. Gonzales, J. D. Mathews, J. H. Elder, and R. L. Walterscheid (2004), A continuum of gravity waves in the Arecibo thermosphere?, *Geophys. Res. Lett.*, *31*, L16801, doi:10.1029/2003GL019376.

Eckermann, S., and C. Marks (1996), An idealized ray model of gravity wave-tidal interactions, *J. Geophys. Res.*, *101*, D16, doi:10.1029/96JD01660.

Fritts, D. C., and M. J. Alexander (2003), Gravity wave dynamics and effects in the middle atmosphere, *Rev. Geophys.*, *41*, 1003, doi:10.1029/2001RG000106.

Fritts, D. C., and S. Vadas (2008), Gravity wave penetration into the thermosphere: Sensitivity to solar cycle variations and mean winds, *Ann. Geophys.*, *26*, 3841–3861, doi:10.5194/angeo-26-3841-2008.

Fukushima, D., K. Shiokawa, Y. Otsuka, and T. Ogawa (2012), Observation of equatorial nighttime medium-scale traveling ionospheric disturbances in 630-nm airglow images over 7 years, *J. Geophys. Res.*, *117*, A10324, doi:10.1029/2012JA017758.

Hajkowicz, L. A. (1990), A global study of large scale travelling ionospheric disturbances (TIDs) following a step-like onset of auroral substorms in both hemispheres, *Planet. Space Sci.*, *38*, 913–923.

Harkrider, D. G. (1964), Theoretical and observed acoustic-gravity waves from explosive sources in the atmosphere, *J. Geophys. Res.*, *69*, 5295–5321.

Hickey, M. P., and K. D. Cole (1987), A quartic dispersion equation for internal gravity waves in the thermosphere, *J. Atmos. Terr. Phys.*, *49*, 889–899.

Hickey, M. P., and K. D. Cole (1988), A numerical model for gravity wave dissipation in the thermosphere, *J. Atmos. Terr. Phys.*, *50*, 689–697.

Hickey, M. P., G. Schubert, and R. L. Walterscheid (2009), The propagation of tsunami-driven gravity waves into the thermosphere and ionosphere, *J. Geophys. Res.*, *114*, A08304, doi:10.1029/2009JA014105.

Hines, C. O. (1960), Internal atmospheric gravity waves at ionospheric heights, *Can. J. Phys.*, *38*, 1441–1481.

Hines, C. O. (1967), On the nature of travelling ionospheric disturbances launched by low-altitude nuclear explosions, *J. Geophys. Res.*, *72*, 1877–1882.

Hocke, K., and K. Schlegel (1996), A review of atmospheric gravity waves and traveling ionospheric disturbances, *Ann. Geophys.*, *14*, 917–940.

Hocke, K., and T. Tsuda (2001), Gravity waves and ionospheric irregularities over tropical convection zones observed by GPS/MET radio occultation, *Geophys. Res. Lett.*, *28*, 2815–2818.

Holton, J. R., and M. J. Alexander (1999), Gravity waves in the mesosphere generated by tropostric convection, *Tellus*, *51A-B*, 45–58.

Holton, J. R., J. H. Beres, and X. Zhou (2002), On the vertical scale of gravity waves excited by localized thermal forcing, *J. Atmos. Sci.*, *59*, 2019–2023.

Horinouchi, T., T. Nakamura, and J.-I. Kosaka (2002), Convectively generated mesoscale gravity waves simulated throughout the middle atmosphere, *Geophys. Res. Lett.*, *29*(21), 2007, doi:10.1029/2002GL016069.

Hung, R. J., and J. P. Kuo (1978), Ionospheric observation of gravity-waves associated with hurricane Eloise, *J. Geophys.*, *45*, 67–80.

Kundu, P. (1990), *Fluid Mechanics*, 638 pp., Academic Press, San Diego.

Lane, T. P., M. J. Reeder, and T. L. Clark (2001), Numerical modeling of gravity waves generated by deep tropical convection, *J. Atmos. Sci.*, *58*, 1249–1274.

Lane, T. P., R. D. Sharman, T. L. Clark, and H.-M. Hsu (2003), An investigation of turbulence generation mechanisms above deep convection, *J. Atmos. Sci.*, *60*, 1297–1321, doi:10.1175/1520-0469.

Lighthill, J. (1978), *Waves in Fluids*, 504 pp., Cambridge University Press, Cambridge, p. 327 in Sec. 4.6.

Lindzen, R. S. (1981), Turbulence and stress owing to gravity wave and tidal breakdown, *J. Geophys. Res.*, *86*(C10), 9707–9714.

Liu, H.-L. (2000), Temperature changes due to gravity wave saturation, *J. Geophys. Res.*, *105*, 12329–12336.

Liu, H.-L., and S. L. Vadas (2013), Large-scale ionospheric disturbances due to the dissipation of convectively-generated gravity waves over Brazil, *J. Geophys. Res.*, doi:10.1002/jgra.50244, in press.

Nicolls, M. J., and C. J. Heinselman (2007), Three dimensional measurements of traveling ionospheric disturbances with the Poker Flat Advanced Modular Incoherent Scatter Radar, *Geophys. Res. Lett.*, *34*, L21104, doi:10.1029/2007GL031506.

Nicolls, M. J., S. L. Vadas, J. W. Meriwether, M. G. Conde, and D. Hampton (2012), The phases and amplitudes of gravity waves propagating and dissipating in the thermosphere: Application to measurements over Alaska, *J. Geophys. Res.*, *117*, A05323, doi:10.1029/2012JA017542.

Occhipinti, G., P. Lognonné, E. Alam Kherani, and H. Hébert (2006), 3D waveform modeling of ionospheric signature induced by the 2004 Sumatra tsunami, *Geophys. Res. Lett.*, *33*, L20104, doi:10.1029/2006GL026865.

Occhipinti, G., A. Kherani, and P. Lognonné (2008), Geomagnetic dependence of ionospheric disturbances induced by tsunamigenic internal gravity waves, *Geophys. J. Int.*, doi:10.1111/j.1365-246X.2008.03760.X.

Occhipinti, G., P. Coisson, J. J. Makela, S. Allgeyer, A. Kherani, H. Hebert, and P. Lognonné (2011), Three-dimensional numerical modeling of tsunami-related internal gravity waves in the Hawaiian atmosphere, *Earth Planets Space*, *63*, 847–851.

Oliver, W. L., Y. Otsuka, M. Sato, T. Takami, and S. Fukao (1997), A climatology of *F* region gravity wave propagation over the middle and upper atmosphere radar, *J. Geophys. Res.*, *102*, 14,499–14,512.

Pandya, R. E., and M. J. Alexander (1999), Linear stratospheric gravity waves above convective thermal forcing, *J. Atmos. Sci.*, *56* (14), 2434–2446.

Piani, C., D. Durran, M. J. Alexander, and J. R. Holton (2000), A numerical study of three dimensional gravity waves triggered by deep tropical convection, *J. Atmos. Sci.*, *57*, 3689–3702.

Pierce, A. D., and S. C. Coroniti (1966), A mechanism for the generation of acoustic-gravity waves during thunderstorm formation, *Nature*, *210*, 1209–1210, doi:10.1038/2101209a0.

Pitteway, M. L. V., and C. O. Hines (1963), The viscous damping of atmospheric gravity waves, *Can. J. Phys.*, *41*, 1935–1948.

Press, W. H., S. A. Teukolsky, W. T. Vetterling, and B. P. Flannery (1992), *Numerical Recipes in Fortran,* 2nd ed., 963 pp., Cambridge University Press, Cambridge.

Preusse, P., S. D. Eckermann, and M. Ern (2008), Transparency of the atmosphere to short horizontal wavelength gravity waves, *J. Geophys. Res.*, *113*, D24104, doi:10.1029/2007JD009682.

Richmond, A. D. (1978), Gravity wave generation, propagation, and dissipation in the thermosphere, *J. Geophys. Res.*, *83*, 4131–4145.

Rishbeth, H., and O. K. Garriott (1969), *Introduction to Ionospheric Physics*, 331 pp., Academic Press, New York.

Roble, R. G., and E. C. Ridley (1994), A thermosphere-ionosphere-mesosphere-electrodynamics general circulation model (TIME-GCM): Equinox solar cycle minimum simulations (30-500km), *Geophys. Res. Lett.*, *21*, 417–420.

Rolland, L. M., G. Occhipinti, P. Lognonné, and A. Loevenbruck (2010), Ionospheric gravity waves detected offshore Hawaii after tsunamis, *Geophys. Res. Lett.*, *37*, L17101, doi:10.1029/2010GL044479.

Röttger, J. (1977), Travelling disturbances in the equatorial ionosphere and their association with penetrative cumulus convection, *J. Atmos. Terr. Phys.*, *39*, 987–998.

Shiokawa, K., Y. Otsuka, and T. Ogawa (2006), Quasiperiodic southward moving waves in 630-nm airglow images in the equatorial thermosphere, *J. Geophys. Res.*, *111*, A06301, doi:10.1029/2005JA011406.

Smith, S. A., D. C. Fritts, and T. E. Vanzandt (1987), Evidence for a saturated spectrum of atmospheric gravity waves, *J. Atmos. Sci.*, *44*, 1404–1410.

Song, I.-S., H.-Y. Chun, and P. P. Lane (2003), Generation mechanisms of convectively forced internal gravity waves and their propagation to the stratosphere, *J. Atmos. Sci.*, *60*, 1960–1980.

Stull, R. B. (1976), Internal gravity waves generated by penetrative convection, *J. Atmos. Sci.*, *33*(7), 1279–1286.

Sun, L., W. Wan, F. Ding, and T. Mao (2007), Gravity wave propagation in the realistic atmosphere based on a three-dimensional transfer function model, *Ann. Geophys.*, *25*, 1979–1986.

Vadas, S. L., and D. C. Fritts (2001), Gravity wave radiation and mean responses to local body forces in the atmosphere, *J. Atmos. Sci.*, *58*, 2249–2279.

Vadas, S. L., D. C. Fritts, and M. J. Alexander (2003), Mechanism for the generation of secondary waves in wave breaking regions, *J. Atmos. Sci.*, *60*, 194–214.

Vadas, S. L., and D. C. Fritts (2004), Thermospheric responses to gravity waves arising from mesoscale convective complexes, *J. Atmos. Sol. Terr. Phys.*, *66*, 781–804.

Vadas, S. L., and D. C. Fritts (2005), Thermospheric responses to gravity waves: Influences of increasing viscosity and thermal diffusivity, *J. Geophys. Res.*, *110*, D15103, doi:10.1029/2004JD005574.

Vadas, S. L., and D. C. Fritts (2006), Influence of solar variability on gravity wave structure and dissipation in the thermosphere from tropospheric convection, *J. Geophys. Res.*, *111*, A10S12, doi:10.1029/2005JA011510.

Vadas, S. L. (2007), Horizontal and vertical propagation and dissipation of gravity waves in the thermosphere from lower atmospheric and thermospheric sources, *J. Geophys. Res.*, *112*, A06305, doi:10.1029/2006JA011845.

Vadas, S. L., and M. J. Nicolls (2009), Temporal evolution of neutral, thermospheric winds and plasma response using PFISR measurements of gravity waves, *J. Atmos. Sol. Terr. Phys.*, *71*, 740–770.

Vadas, S. L., and D. C. Fritts (2009), Reconstruction of the gravity wave field from convective plumes via ray tracing, *Ann. Geophys.*, *27*, 147–177.

Vadas, S. L., and H.-L. Liu (2009), The generation of large-scale gravity waves and neutral winds in the thermosphere from the dissipation of convectively-generated gravity waves, *J. Geophys. Res.*, *114*, A10310, doi:10.1029/2009JA014108.

Vadas, S. L., M. J. Taylor, P.-D. Pautet, P. A. Stamus, D. C. Fritts, H.-L. Liu, F. T. Sao Sabbas, V. T. Rampinelli, P. Batista, and H. Takahashi (2009a), Convection: The likely source of medium-scale gravity waves observed in the OH airglow layer near Brasilia, Brazil, during the SpreadFEx Campaign, *Ann. Geophys.*, *27*, 231–259.

Vadas, S. L., J. Yue, C.-Y. She, P. A. Stamus, and A. Liu (2009b), A model study of the effects of winds on concentric rings of gravity waves from a convective plume near Fort Collins on 11 May 2004, *J. Geophys. Res.*, *114*, D06103, doi:10.1029/2008JD010753.

Vadas, S. L., and G. Crowley (2010), Sources of the traveling ionospheric disturbances observed by the ionospheric TIDDBIT sounder near Wallops Island on October 30, 2007, *J. Geophys. Res.*, *115*, A07324, doi:10.1029/2009JA015053.

Vadas, S. L., and H.-L. Liu (2011), Neutral winds and densities at the bottomside of the *F* layer from primary and secondary gravity waves from deep convection, in *Aeronomy of the Earth's Atmosphere and Ionosphere,* IAGA Special Sopron Book Series, edited by M. A. Abdu, D. Pancheva, and A. Bhattacharyya, vol. 2, pp. 131–139, Springer, New York.

Vadas, S. L., and M. J. Nicolls (2012), The phases and amplitudes of gravity waves propagating and dissipating in the thermosphere: Theory, *J. Geophys. Res.*, *117*, A05322, doi:10.1029/2011JA017426.

Vadas, S. L., J. Yue, and T. Nakamura (2012), Mesospheric concentric gravity waves generated by multiple convection storms over the North America Great Plain, *J. Geophys. Res.*, *117*, D7, doi:10.1029/2011JD017025.

Vadas, S. L. (2013), Compressible f-plane solutions to body forces, heatings, and coolings, and application to the primary and secondary gravity waves generated by a deep convective plume, *J. Geophys. Res.*, doi:10.1002/jgra.50163, in press.

Walterscheid, R. L. (1981), Dynamical cooling induced by dissipating internal gravity-waves, *J. Geophys. Res.*, *8*, 1235–1238.

Walterscheid, R. L., G. Schubert, and D. G. Brinkman (2001), Small-scale gravity waves in the upper mesosphere and lower thermosphere generated by deep tropical convection, *J. Geophys. Res.*, *106*, D23, 31825–31832

Yiğit, E., A. D. Aylward, and A. S. Medvedev (2008), Parameterization of the effects of vertically propagating gravity waves for thermosphere general circulation models: Sensitivity study, *J. Geophys. Res.*, *113*, D19106, doi:10.1029/2008JD010135.

Yiğit, E., A. S. Medvedev, A. D. Aylward, P. Hartogh, and M. J. Harris (2009), Modeling the effects of gravity wave momentum deposition on the general circulation above the turbopause, *J. Geophys. Res.*, *114*, D07101, doi:10.1029/2008JD011132.

Yiğit, E., and A. S. Medvedev (2009), Heating and cooling of the thermosphere by internal gravity waves, *Geophys. Res. Lett.*, *36*, L14807, doi:10.1029/2009GL038507.

Zhu, X., and J. R. Holton (1987), Mean fields induced by local gravity-wave forcing in the middle atmosphere, *J. Atmos. Sci.*, *44*, 620–630.